




# WDPHOTTools – A White Dwarf Photometric Toolkit in Python

M. C. Lam<sup>1,2</sup> \*, K. W. Yuen<sup>3</sup>, M. J. Green<sup>1</sup> , and W. Li<sup>1</sup> 

<sup>1</sup>*School of Physics and Astronomy, Tel Aviv University, Tel Aviv, Israel 69978*

<sup>2</sup>*Astrophysics Research Institute, Liverpool John Moores University, IC2, LSP, 146 Brownlow Hill, Liverpool L3 5RF, UK*

<sup>3</sup>*Department of Ophthalmology & Visual Sciences, Faculty of Medicine, The Chinese University of Hong Kong*

Accepted 2022. Received 2022; in original form 2022

## ABSTRACT

From data collection to photometric fitting and analysis of white dwarfs to generating a white dwarf luminosity function requires numerous Astrophysical, Mathematical and Computational domain knowledge. The steep learning curve makes it difficult to enter the field, and often individuals have to reinvent the wheel to perform identical data reduction and analysis tasks. We have gathered a wide range of publicly available white dwarf cooling models and synthetic photometry to provide a toolkit that allows (1) visualisation of various models, (2) photometric fitting of a white dwarf with or without distance and reddening, and (3) the computing of white dwarf luminosity functions with a choice of initial mass function, main sequence evolution model, star formation history, initial-final mass relation, and white dwarf cooling model. We have recomputed and compared the effective temperature of the white dwarfs from the Gaia EDR3 white dwarf catalogue. The two independent works show excellent agreement in the temperature solutions.

**Key words:** methods: data analysis – software: data analysis – software: public release – stars: luminosity function, mass function – (stars:) white dwarfs

## 1 INTRODUCTION

White dwarfs (WDs) are the final stage of stellar evolution of main sequence (MS) stars with zero-age MS (ZAMS) mass less than  $\sim 8M_{\odot}$  (Kippenhahn et al. 2013). Since this mass range encompasses the vast majority of stars in the Galaxy, these degenerate remnants are the most common final product of stellar evolution, thus providing a good sample to study the history of stellar evolution and star formation at the earliest time of the Galaxy. In this state, there is little nuclear burning to replenish the energy they radiate away. As a consequence, the luminosity and temperature decrease monotonically with time. The electron degenerate nature means that a WD with a typical mass of  $0.6M_{\odot}$  has a similar size to the Earth, giving rise to their high densities, low luminosities, and large surface gravities.

The use of the white dwarf luminosity function (WDLF) as a cosmochronometer was first introduced by Schmidt (1959). Given the finite age of the Galaxy, there is a minimum temperature below which no white dwarfs can reach in a limited cooling time. This limit translates to an abrupt downturn in the WDLF at faint magnitudes. Evidence of such behaviour was observed by Liebert et al. (1979), however, it was not clear at the time whether it was due to incompleteness in the observations or to some defect in the theory (e.g., Iben & Tutukov 1984). A decade later, Winget et al. (1987) gathered concrete evidence for the downturn and estimated the age<sup>1</sup> of the disc to be  $9.3 \pm 2.0$  Gyr (see also Liebert et al. 1988).

While most studies focused on the combined Galactic thin and thick discs (Liebert et al. 1989; Wood 1992; Oswalt & Smith 1995; Leggett et al. 1998; Knox et al. 1999; Giammichele et al. 2012; Gaia Collaboration et al. 2021b), some worked with the combined discs and the stellar halo (Harris et al. 2006; Munn et al. 2017; Lam et al. 2019). There was one attempt in disentangling the thin disc, thick disc and the stellar halo component WDLFs (Rowell & Hambly 2011).

Most WDs have similar broadband colour to main sequence stars, so they cannot be identified using photometry alone. They are found from UV-excess, large proper motion and/or parallax. Because of the strongly peaked surface gravity distribution of WDs, photometric fitting for their intrinsic properties is possible by assuming a surface gravity. WDs fitted in such a way are statistically useful provided that the sample is not strongly biased. This is demonstrated in various studies comparing photometric and spectroscopic solutions to calibrate the atmosphere model (Genest-Beaulieu & Bergeron 2019a,b), as well as from the agreeing shapes of the WDLFs from spectroscopic and photometric samples. The Gaia satellite provides parallactic measurements for over a billion point sources (Gaia Collaboration et al. 2021a; Bailer-Jones et al. 2021) of which 359 000 are high confidence WD candidates (Gentile Fusillo et al. 2021, hereafter, GF21). The availability of parallaxes allows much more accurate fitting, particularly, without knowing the surface gravity for the photometric sample. This has completely revolutionized the field of WD sciences. In the forthcoming decade, the Simonyi Survey Telescope at the Vera C. Rubin Observatory will continue to discover more WDs at fainter magnitudes, but only accompanied by proper motion measurement at best at the faintest magnitudes. Furthermore, at those magnitudes, it is infeasible to collect spectra for most of them and thus studies will mostly rely on photometric methods.

\* Contact e-mail: lam@mail.tau.ac.il

<sup>1</sup> “Age” refers to the total time since the oldest WD progenitor arrived at the zero-age main sequence.

In this generation of user-side astronomical data handling and analysis, as well as in the computing courses for scientists, PYTHON is among the most popular languages due to its ease to use with a relatively shallow learning curve, readable syntax and a simple way to ‘glue’ different pieces of software together. Its flexibility to serve as a scripting and an object-oriented language makes it useful in many use cases: demonstrating with visual tools with little overhead, prototyping, and web-serving, and it can be compiled if wanted. This broad range of functionality and high-level usage make it relatively inefficient. However, Python is an excellent choice of language to build wrappers over highly efficient and well-established codes. In fact, some of the most used packages, SCIPY (Virtanen et al. 2020) and NUMPY (Harris et al. 2020), are written in FORTRAN and C, respectively. WDPHOTTOOLS depends heavily on these two highly optimised and matured packages to deliver the desired efficiency.

This paper is organised as follows: in Section §2, we describe the software structure and development process. Section §3 describes the model formatter. Section §4 covers the photometric fitting procedures and the overview of the model used. It also explains the construction of a theoretical luminosity function including some descriptions of the models available. Section §5 goes through the other tools that are essential to the software. We describe some auxiliary tools that is also available with this toolkit in Section §6, and we summarise this work in Section §7.

Throughout this work, we use  $m$  to denote apparent magnitude,  $M$  for absolute magnitude, curly  $\mathcal{M}$  to denote mass, where  $\mathcal{M}_i$  for the (initial) ZAMS mass, and  $\mathcal{M}_f$  for the (final) WD mass.

## 2 SOFTWARE AND DEVELOPMENT ORGANISATION

The goal of this work is to ease researchers the effort in reinventing the wheel for trivial, repetitive but essential first steps in many aspects of data analysis for WD science. WDPHOTTOOLS allows a simple setup to compare results from different choices of models. We note that this work is only suitable for the analysis of the most common types of WDs. It is not advisable to perform analysis on any WDs that are suspected to have evolved with companion, or with atypical core and/or atmospheric composition. There is already a spectroscopic version for a similar purpose, the WDTOOLS<sup>2</sup> (Chandra et al. 2020). While we are drawing an analogy between the two pieces of software, we would like to emphasise that their implementation starts from a lower level that directly makes use of the output products of the stellar evolution models. The synthetic photometry part of the WDPHOTTOOLS begins with pre-computed tables in which the filter profiles have already been convolved with the model spectra, with the normalisation (absolute magnitude) of the photometry determined based on the mass-radius relation from their simulations. Future development of WDPHOTTOOLS will move away from this (see Section §7).

WDPHOTTOOLS can generate colour-colour diagrams, colour-magnitude diagrams in various photometric systems, plot cooling profiles from different models, and compute theoretical WDLF based on the built-in or supplied models. The core parts of this work are three-fold: (1) the tailored-formatters that handle the output models from various works in the format as they were generated and downloaded. This allows the software to be updated to handle future releases of the models easily. They are written as two base classes: `AtmosphereModelReader` and `CoolingModelReader`; (2) photometric fitter (`WDFitter` class), that solves for the WD parameters

based on the photometry, with or without distance and reddening; and (3) to generate white dwarf luminosity function in bolometric magnitudes or in any of the photometric systems available from the atmosphere models (with the WDLF class).

We host our source code on Github<sup>3</sup>, which provides version control and other utilities to facilitate the development; the numbered releases are also deposited on Zenodo to allow referencing of a specific version<sup>4</sup>. It offers issue and bug tracking, high-level project management, automation with Github Actions upon each commit for:

- (i) Continuous Integration (CI) to install the software in Linux, Mac and Windows system, and then perform unit tests with PYTEST (Krekel et al. 2004);
- (ii) generating test coverage report with Coveralls<sup>5</sup> which identifies lines in the script that are missed by the tests;
- (iii) Continuous Deployment (CD) through PyPI that allows immediate availability of the latest software release; and
- (iv) generating application programming interface (API) documentation powered by SPHINX hosted on Read the Docs<sup>6</sup>.

The following is not serving as an API, it is describing some of the key arguments and parameters, as well as the usage that may seem convoluted but is necessary to keep the structure simple without providing multiple methods to perform similar tasks with small adjustments. The model-readers are designed to read the files as they are downloaded from the source, such that the future updates of the models provided by the same research group should be a straightforward process in extending the model list. The materials that have gone into the classes and modules are described in §3 to §6 alongside with the usage of those classes and modules. We summarise this work in §7.

## 3 FORMATTERS

There are two classes of model readers, one is for reading the synthetic photometry computed from the Montreal DA/DB atmosphere models; the other one is a formatter that handled the different formats in the output files from different providers.

### Synthetic Photometry

The publicly available Montreal models<sup>7</sup>, provide synthetic photometry of WDs over a smooth grid of wide ranges of temperature and surface gravity. The tables are provided with bolometric and absolute magnitudes on various photometric systems in pure hydrogen (DA) and pure-helium (DB) atmospheres and in the range of  $\log(g) = 7.0 - 9.0$ , as well as the effective temperature and total cooling time (though this grid is sparse compared to their complementary cooling model grids). The photometric systems include the Johnson-Kron-Cousins ( $U, B, V, R \& I$ ), Two Micron All Sky Survey (2MASS)  $J, H \& K_s$ , Mauna Kea Observatory (MKO)  $Y, J, H \& K$ , Wide-field Infrared Survey Explorer (WISE)  $W1, W2, W3 \& W4$ , Spitzer Space Telescope Infrared Array Camera (IRAC)  $[3.6], [4.5], [5.8] \& [8.0]\mu\text{m}$ , Sloan Digital Sky Survey (SDSS)  $u, g, r, i \& z$ , Panoramic Survey Telescope

<sup>2</sup> <https://github.com/vedantchandra/wdtools>

<sup>3</sup> <https://github.com/cylamarco/WDPHOTTOOLS>

<sup>4</sup> <https://doi.org/10.5281/zenodo.6595029>

<sup>5</sup> <https://coveralls.io/github/cylamarco/WDPHOTTOOLS>

<sup>6</sup> <https://wdphottools.readthedocs.io>

<sup>7</sup> <https://www.astro.umontreal.ca/~bergeron/CoolingModels/>

and Rapid Response System (Pan-STARRS 1)  $g, r, i, z$  &  $y$ , Gaia  $G$ ,  $G_{BP}$  &  $G_{RP}$ , and Galaxy Evolution Explorer (GALEX)  $FUV$  and  $NUV$ .

The stellar masses and cooling ages are based on the latest generation of evolution sequences (Bédard et al. 2020) with the choices of thick ( $q_H \equiv \frac{M_H}{M_*} = 10^{-4}$ ) and thin ( $q_H = 10^{-10}$ ) hydrogen layers that are referred to as the pure-hydrogen and pure-helium model atmospheres, respectively. Details of the colour calculations are described in Bergeron et al. (1995) and Holberg & Bergeron (2006). The DA grid covers a temperature range  $T_{\text{eff}} = 2\,500 - 150\,000$  K while the DB grid covers  $T_{\text{eff}} = 3\,250 - 150\,000$  K. Both models are computed with surface gravities  $\log(g) = 7.0 - 9.0$  (Blouin et al. 2018; Bédard et al. 2020; Tremblay et al. 2011; Bergeron et al. 2011; Kowalski & Saumon 2006).

### 3.1 Class: AtmosphereModelReader

This class takes care of the formatting of the models. As compared to the cooling model reader, this is a simple reader because only the DA and DB atmosphere types in the same output format are available for a wide range of parameters and in various commonly used broadband filters. After initialisation, the method `list_atmosphere_parameters()` can be used to retrieve the parameters available for interpolation with `interp_am()`. By default, it is initialised as a DA atmosphere interpolator providing the interpolated  $G$  band magnitudes in the Gaia DR3 photometric system (dependent), parameterised in  $\log g$  and  $M_{\text{bol}}$  (independent). We name the arguments dependent and independent using the common terminology in mathematical modelling and experimental science: the variables defining the axes of the interpolation are the *independent* variables, and the variable being interpolated over is the *dependent* variable. The number of independent variables can be one or two. In the former, the argument `logg` has to be provided which is defaulted to 8.0. There are two choices of interpolator: `scipy.interpolate.CloughTocher2DInterpolator()` and `scipy.interpolate.RBFInterpolator()`. The former is faster but it is less stable at the grid boundaries, and it also does not natively support extrapolation. The latter is slower<sup>8</sup> but it is more stable against irregularly sampled data as well as at the boundaries. It also supports extrapolation natively. The choice depends on the usage. The default is choosing `CloughTocher2DInterpolator` because it would be usable with older distribution of `SCIPY`. Fine control of the interpolator can be performed using keyword arguments. The cooling tracks on a colour-magnitude diagram are shown for the Montreal DA model in Figure 1.

### 3.2 Class: CoolingModelReader

The reader for the 24 cooling models from sixteen pieces of work is more complex because the outputs from different models are organised differently. These are all handled in the background and users only need to choose among the models. Similar to the `AtmosphereModelReader`, after initialisation, the method `list_cooling_model()` can be used to retrieve the available models and then the parameters available for interpolation from those models can be retrieved using `list_cooling_parameters()`.

<sup>8</sup> This method is available since `SCIPY` version 1.7, however, we strongly recommend using version 1.9 or above where there is a significant performance gain in the `RBFInterpolator`.

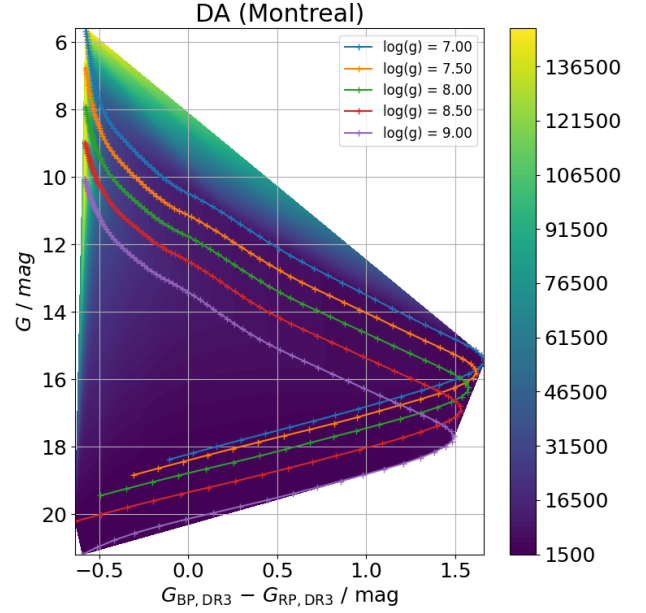


**Figure 1.** Default figures showing the cooling tracks at different surface gravities in the Gaia  $G$ ,  $G_{BP}$  and  $G_{RP}$  filters. The colours scale shows the effective temperature.

With the chosen model name and parameter names, an interpolator can be built using the method `interp_cm()`, which will use the appropriate formatter to read the model files already contained in the package. In this class, the same two interpolators, `scipy.interpolate.CloughTocher2DInterpolator()` and `scipy.interpolate.RBFInterpolator()`, are available for use. See Table 1 for the complete listing of the available models.

## 4 PHOTOMETRIC FITTING

Photometric fitting with synthetic broadband photometry has been the common practice in getting the first guess of the atmospheric properties of white dwarf candidates, or any unknown astronomical source. Photometry from multiple filters and parallaxic measurements can improve on the fitting accuracy. It may seem to become obsolete in the era of Gaia as most white dwarfs have measured parallaxes. However, the faint targets with respect to any survey are always going to remain a challenge as the uncertainties in all the observables are going to be significant. Hence, photometric fitting will continue to serve as a useful method in the future. Once VRO starts producing WD candidates at faint magnitudes, they would be far beyond the capabilities of most spectrographs. The few spectrographs mounted on 10 m+ telescopes are a rare resource for follow-up and it would be not possible to obtain spectra to confirm a sizeable sample of WD candidates. We will have to rely mostly on photometric method again, and without any parallaxic measurements.

### 4.1 Class: WDFitter

This class inherits from the `AtmosphereModelReader`. For basic usage, users are only required to provide the atmospheric type(s), the magnitudes and uncertainties in the respective filters. For more advanced usage, other fine-tuning can be performed by providing

distance, extinction, independent variables<sup>9</sup>, choice of interpolator and their fine-tuning parameters, minimisers and their fine-tuning parameters, or solution refinement within a bounding box (only if EMCEE was used). A few arguments are worth extra attention because of the similar terms used by different methods. We are only pointing out the potential confusion with the arguments, the detailed usage should be referred to the API document itself:

(i) The argument `extinction_convolved` refers to the use of tabulated values from convolving the filter response function with DA spectra to compute the extinction corrected for the spectral shape (see also Section §4.3 and Figure 3) When it is set to `False`, it interpolates the tabulated values from the Appendix of [Schlafly & Finkbeiner \(2011\)](#).

(ii) `kind` is the kind of interpolation for the extinction.

(iii) `logg` is used *if only* one independent variable is provided.

(iv) `method` sets the choice from the 3 minimizers.

(v) There are 5 keyword arguments that can be used to perform fine control over the minimizer and interpolator: `kwargs_for_RBF`, `kwargs_for_CT`, `kwargs_for_minimize`, `kwargs_for_least_squares` and `kwargs_for_emcee`.

This class also comes with two diagnostic plots. The first one, `show_best_fit()` overplots the best fit photometry corrected for the (fitted) distance (and reddening) with the observed data. The second one, `show_corner_plot()`, shows the probability distribution functions from the MCMC sampling [2](#).

Photometric fitting can be performed by minimizing the  $\chi^2$  with any method supported by `scipy.optimize.minimize()`, `scipy.optimize.least_squares()` or with a Markov chain Monte Carlo method powered by `emcee` ([Foreman-Mackey et al. 2013](#)) with the option to refine the solution with `minimize()` at the end using the 50<sup>th</sup>-percentile as the initial guess and bounding the fit within N-sigma uncertainty limit (user-defined). The uncertainties are not computed when using the `minimize()` method, while the latter two do estimate the uncertainty as part of the minimisation procedure. At high temperatures ( $T_{\text{eff}} \geq 11\,000\text{ K}$ ), the differences in mass inferred from pure H or pure He models are of the order of  $\sim 0.1\,M_{\odot}$ . However, the differences between the pure He and mixed H/He solutions in the same temperature range are completely negligible. At lower temperatures, the atmospheric compositions have much stronger effects. When fitted with pure He models, the average mass of a population decreases; the average mass decreases further when fitted with the mixed H/He models. The above-average-mass WDs in the temperature range of  $6\,000 - 10\,000\text{ K}$  have an average mass above  $0.7\,M_{\odot}$  when fitted with pure hydrogen model, but this drops to  $\sim 0.6\,M_{\odot}$  when fitted with mixed H/He models ([Bergeron et al. 2019](#)). Below  $\sim 6\,000\text{ K}$ , optical spectra are not particularly useful in distinguishing the atmosphere type, because hydrogen absorption lines *start* to disappear, while the helium lines disappear as early as at  $\sim 9\,000\text{ K}$  ([Rolland et al. 2018](#)). However, the broad spectral features, namely the collisionally induced absorption, in the infrared can distinguish the atmosphere type (see Figure 12 of [Blouin et al. 2017](#)). Therefore, readers are reminded to pay particular care when you arrive at a low temperature solution with only optical data.

With  $n$  observables, it is only possible to fit for  $n - 1$  variables. If there are only two photometric bands, it is only possible to fit for one parameter if the *distance is unknown*. By combining 2-band

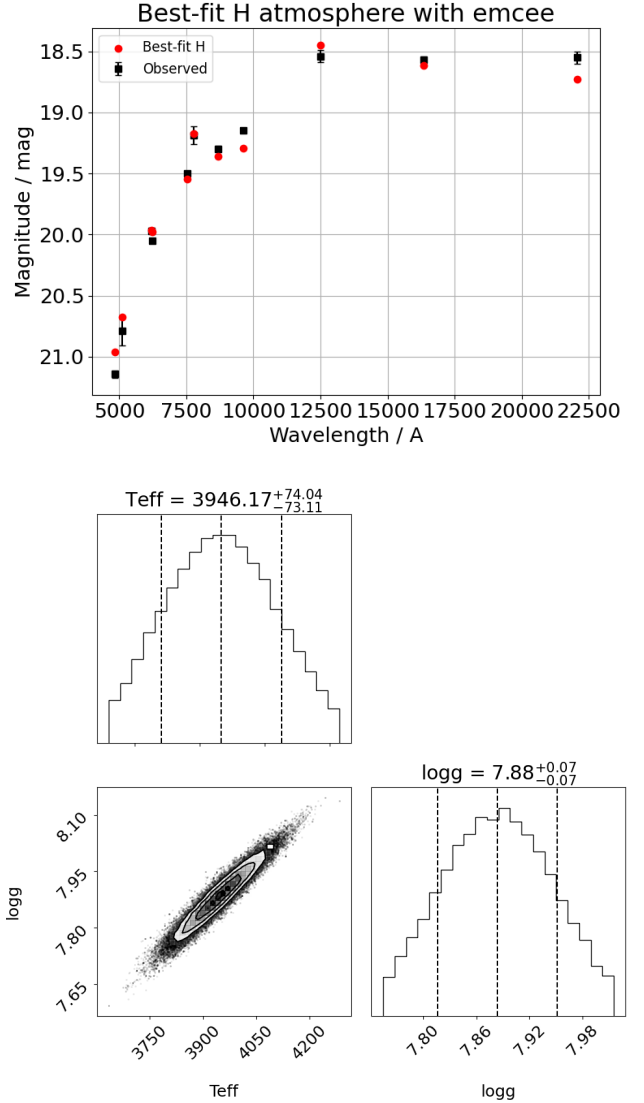


**Figure 2.** Best fit DA solutions found using MCMC with EMCEE and the associated corner plot of the sampling for PSO J1801+6254 ([Lam et al. 2020](#), they found a spectroscopic of  $T_{\text{eff}} = 3550\text{ K}$ ).

photometry *with a distance*, there is enough degree of freedom to fit two parameters.

This does not apply to fitting with or without interstellar reddening because it is merely a one-to-one lookup value, which itself is only a function of distance. When studying a population of WDs that are fitted for the distance, we should compare the photometric distance to the distances measured from other means, e.g. astrometry, spectroscopic distance etc. in order to assess the bias in the fit (e.g. Section §3.2.2 in [Rowell & Hambly 2011](#)).

The effective temperature (and absolute bolometric magnitude) and the solid angle of a source can be obtained when the distance is known, through the relation  $\Omega = \pi R^2 / D^2$ . In the era of Gaia ([Gaia Collaboration et al. 2021a](#)), most WD candidates have their parallaxes measured, and hence the distances derived ([Bailer-Jones et al. 2021](#)). This allows much more reliable photometric fitting with broadband photometry alone, as compared to fitting with an assumed surface gravity (see below). By using an evolutionary model of WDs, the ra-

<sup>9</sup> Fitting using `Mbol` and `Teff` can give slightly different results due to interpolation.



dius and the effective temperature can be used to obtain the mass (and surface gravity). We do not provide a means to use an alternative mass-radius relation of white dwarfs. The fitting is only performed using the relation already adopted in the tables of synthetic photometry.

Even though this is known as the photometric fitting, and values are almost exclusively reported in magnitude, the measurement of the apparent brightness is ultimately performed in electron counts. With good calibration and detector linearity behaviour, it is sufficiently accurate to treat the uncertainties at the flux level. The uncertainty in flux measured has a Gaussian-like error that is symmetrical to both over- and under-estimation of the flux. However, because magnitudes are in the logarithmic space of the flux, the uncertainty in magnitude is no longer symmetrical about the “central” value. Thus fitting directly with magnitude weighted by the magnitude uncertainty leads to a bias: solutions are biased to be over-luminous. For example, at  $\pm 0.1$  mag, the flux ratios are 1.0965 and 0.9120, respectively, corresponding the  $(-)$ 8.8% and  $(+)$ 9.65% change in the flux in the faint and bright end. This only narrows down to  $(-)$ 0.917% and  $(+)$ 0.925% at  $\pm 0.01$  mag level<sup>10</sup>. This effect becomes visually obvious if one is to perform an MCMC sampling and inspect the probability distribution functions. For this reason, in WDPHOTTOOLS, we fit in flux-space where the linear and symmetrical approximation of the uncertainty distribution is more realistic.

For comparison against other work on model fitting, it is very important to state the minimisation/likelihood function. If the functions are different to begin with, it is almost certainly impossible for the recomputed data to have a perfect agreement with the data set that is compared against. Secondly, the different choices (or even versions) of interpolation and minimisation methods will also prevent repeatability. Thus, we detail the likelihood functions and the choice of the interpolators as follows.

## 4.2 Mathematical Construction

We provide three means of fitting. The first two are both finding the minimum  $\chi^2$ , with different minimizers. In the following equations, we use  $m$  and  $f$  to denote apparent magnitude and flux; and  $M$  and  $F$  to denote absolute magnitude and flux. The function to be minimized in these two cases is the square of the weighted difference between model and observation.

$$\left( \frac{F_{\text{model},i} - F_i}{\sigma_{F,i}} \right)^2 \quad (1)$$

where  $F_{\text{model},i}$  is the model flux in filter  $i$ ,  $F$  is the absolute flux (coming from the observed flux adjusted to it would be if it were at a distance of 10 pc), and  $\sigma$  is the combined uncertainty in the flux and distance which can be found from the formal propagation of uncertainties from magnitude and distance to flux with equation 2 and 3:

$$\sigma_F^2 = \sigma_M^2 \times \left[ \frac{\ln(10)F}{2.5} \right]^2 \quad (2)$$

and

$$\sigma_M^2 = \left( \frac{\partial M}{\partial m} \sigma_m \right)^2 + \left( \frac{\partial M}{\partial D} \sigma_D \right)^2 \quad (3)$$

where  $D$  and  $\sigma_D$  are the distance and the corresponding uncertainty. By applying the distance-magnitude relation  $M = m - 5 \log_{10}(D)$ ,

it simplifies to

$$\sigma_M^2 = \sigma_m^2 + \left[ \frac{5}{\ln(10)} \right]^2 \left( \frac{\sigma_D}{D} \right)^2. \quad (4)$$

Substituting in also the flux-magnitude relation, using the parametrisation independent of the response of the photometric system:  $m - m_{\text{ZP}} = -2.5 \log_{10}(F/F_{\text{ZP}})$ , we arrive at the  $\chi^2$  function to be minimized in the magnitude space weighted by the formally propagated uncertainties:

$$\chi^2 = \left[ \frac{2.5}{\ln(10)} \right]^2 \times \sum_i \left\{ \frac{1}{\sigma_{M,i}^2} \left[ \left( \frac{10}{D} \right)^2 \times 10^{\frac{m_i - M_{\text{model},i}}{2.5}} - 1 \right]^2 \right\} \quad (5)$$

The third method we provide is to sample the parameter space with an Markov chain Monte Carlo method. This method is more useful in the case when the uncertainties are large or with missing distance. The likelihood that has to be maximised takes a similar form to Equation 5:

$$\mathcal{L} = -\frac{1}{2} \left[ \frac{2.5}{\ln(10)} \right]^2 \times \sum_i \left\{ \frac{1}{\sigma_{M,i}^2} \left[ \left( \frac{10}{D} \right)^2 \times 10^{\frac{m_i - M_{\text{model},i}}{2.5}} - 1 \right]^2 + \ln(2\pi\sigma_i^2) \right\}. \quad (6)$$

## 4.3 Interstellar Reddening

When interstellar reddening is included in the calculation, the  $\chi^2$  minimisation function becomes

$$\chi^2 = \left[ \frac{2.5}{\ln(10)} \right]^2 \times \sum_i \left\{ \frac{1}{\sigma_{M,i}^2} \left[ \left( \frac{10}{D} \right)^2 \times 10^{\frac{m_i - M_{\text{model},i} - A_i(D)}{2.5}} - 1 \right]^2 \right\} \quad (7)$$

and the likelihood function to be maximised becomes

$$\mathcal{L} = -\frac{1}{2} \left[ \frac{2.5}{\ln(10)} \right]^2 \times \sum_i \left\{ \frac{1}{\sigma_{M,i}^2} \left[ \left( \frac{10}{D} \right)^2 \times 10^{\frac{m_i - M_{\text{model},i} - A_i(D)}{2.5}} - 1 \right]^2 + \ln(2\pi\sigma_i^2) \right\}. \quad (8)$$

where  $A_i$  is the total extinction in filter  $i$  at distance  $D$ . In the case when the distance is known, this is a scale value; when the distance is also to be fitted,  $A$  is not directly provided but instead, it is computed from the  $E(B - V)$  at that distance and a choice of  $R_V$ , which is defaulted to 3.1. The reddening vector can be applied in two ways: (1) it can be approximated by interpolating over the effective wavelengths of the broadband filters<sup>11</sup> available in Table 6 of Schlafly & Finkbeiner (2011); and (2) by treating the spectral energy distribution functions more properly, we convolve the respective filter functions with all the DA models (Tremblay & Bergeron 2009;

<sup>11</sup> CTIO *UBVRI*, UKIRT *JHKL'*, Gunn *griz*, SDSS *ugriz*, PS1 *grizy*, LSST *ugrizy*, DES *grizY* and WFC3 *F218W*, *F225W* and *F275W*. We note that LSST is now renamed Simonyi Survey Telescope, at the Vera Rubin Observatory, but it was printed under the former designation in the referenced article.

<sup>10</sup> A negative change in the magnitude corresponds to an increase in flux.

Koester 2010) available at the Spanish Virtual Observatory<sup>12</sup> following the instructions using equation A1 in the Appendix of Schlafly & Finkbeiner (2011, SF11). We have pre-computed the reddening per unit E(B-V) from  $R_V = 2.1$  to 5.1 in 0.5 step increment, using the Fitzpatrick extinction law (Fitzpatrick 1999) with the extinction<sup>13</sup> package (Barbary 2016), for every theoretical spectrum available over all the filters available from the Montreal synthetic photometry table (see Figure 3). In other words, we have a third (effective temperature) and a fourth (surface gravity) dimension of Table 6 in SF11. Our values are making use of WD spectra instead of using a single spectrum of an MS star with  $\log(Z) = -1.0$ , and  $\log(g) = 4.5$  at 7 000 K in SF11. The synthetic spectra do not cover some of the bluest filters, in such cases, we extend those spectra with blackbody profiles. The grid is stored in CSV format and is ready to be interpolated upon initialisation of this toolkit.

#### 4.4 Fitting Distance

Singly evolved WDs have a surface gravity distribution that strongly peaks at  $\langle \log_{10}(g) \rangle = 7.998 \pm 0.011$ , as was found empirically in the DA sample in SDSS DR16 (Kepler et al. 2021), corresponding to a mean mass of  $\langle M_i \rangle = 0.618 \pm 0.006 M_\odot$ . When studying a large sample of WDs, fitting the photometric distances for the study of a population is still useful when reporting an averaged quantity as the final results. The distributions of the solution are, however, mostly statistical noise and not representative to the true distribution when both the strongly degenerate parameters: surface gravity and distance are fitted simultaneously. Equation 1 and 6 are reused in this case, however, the distance modulus, which is a function of distance, becomes a free parameter to be fitted.

#### 4.5 Comparison against EDR3 catalogue of WDs

The catalogue available from GF21 has presented an excellent sample of WDs for comparison to validate our photometric fitting. There is a slight difference between our photometric fitting methodology and that of GF21: in this work, we are correcting for the interstellar reddening at the instantaneous temperature and surface gravity in each iteration of the fit, as opposed to using a global average of the extinction per filter ( $A_G = 0.835 A_V$ ,  $A_{G_{BP}} = 0.6496 A_V$ , and  $A_{G_{RP}} = 1.13894 A_V$ ). The underlying models also differ slightly as the code base diverged slightly with time<sup>14</sup>.

As the spectral energy distribution function changes in the flux density within the broadband filter, the total extinctions of a hotter object are large because of more bluer photons are being extinguished compared to a cooler object. This is measureable within the wavelength range of a broadband filter. The effect is small but not negligible<sup>15</sup> (see also Section § 4.3 and § 6). It is clearly shown in Figure 3 that the differences in the extinction in the Gaia filters are much larger than those in the narrower UBVRI filters. The effect is also slightly stronger in the blue end because of the larger change in the spectral shape as temperature changes from 30 000 K to 5 000 K. Therefore,

we convolve the filter profile with the DA spectra to provide a table of pre-computed extinction coefficient as a function of temperature and surface gravity to allow more accurate reddening correction.

For the above reasons, some scatter is expected when the fitted values from the two works are compared against each other. Particularly among the hotter WDs, their colours deviate much more from the global average than the average population does. Their blue spectral energy distribution should be more extinguished than cooler WDs ( $G_{BP}$  has a much larger spread than  $G_{RP}$ ). Otherwise, we follow as closely to their analysis method as possible: the solutions are fitted with the three Gaia filters, distance, and reddening with using the catalogued values as provided from their work. The distribution of the fitted effective temperatures are aligned well with the identity line, the Pearson correlation coefficient of the fitted effective temperature (for all WDs that have valid solutions fitted regardless of the quality of fit) is 0.95 between this and GF21. We are only displaying fitted results above 3 500 K, in line with the GF21 criteria when publishing their catalogue.

### 5 WHITE DWARF LUMINOSITY FUNCTION

A WDLF is the number density of WD as a function of luminosity. It is an evolving function with time, and it is a common tool for deriving the age of a stellar population. Its shape and normalisation are determined from only a few parameters. Winget et al. (1987) compared an observed WDLF derived from the Luyten Half-Second (LHS) catalogue with a theoretical WDLF to obtain an estimate of the age of the Galaxy for the first time with this technique. Noh & Scalo (1990) examined WDLFs with various SFH scenarios. They showed that WDLF is a sensitive probe of the star formation history (SFH) as it shows signatures of irregularities in the SFH such as bursts and lulls. Rowell (2013) took it further to address this inverse problem mathematically and showed some success in recovering the SFH of the solar neighbourhood when compared against SFH computed from other methods. By decomposing the disks and halo components of the Milky Way, we can have an independent view of the past SFH revealed by only the WD populations, where they are most useful in deriving the SFH of old stellar populations (Rowell & Hambly 2011; Lam 2017).

he construction of a WDLF is intuitively: stars were formed in a distribution of mass ( $M_i$ ), described by the initial mass function (IMF,  $\phi$ ). Then, they spend their lifetime ( $t_{MS}$ ) carrying out nuclear burning, and the time they spend depends mainly on their mass. Towards the end stage of stellar evolution stars shed most of the atmosphere, which is modelled by the initial-final mass relation (IFMR,  $\zeta$ ). Once they have become WDs, all that is left is to know how long it has been cooling ( $t_{cool}$ ) in order to reach the current luminosity.

However, to encompass all these physical processes in an integral even with pre-computed look-up table, the construction of a theoretical WDLF is computationally expensive because of the large dynamic range of varies quantities over the total evolution time. An integrator has to use fine steps to achieve the required precision. The use of interpolation over the pre-computed lookup tables has already significantly reduced the computation time. But the repeated calling of multiple interpolate objects inside an integral still requires a few minutes to compute a single WDLF (at a magnitude resolution of 0.1 mag) using a single typical computer processor thread. We have carefully interpolated and integrated over the model grids, because they are both susceptible to significant rounding errors given the huge dynamic ranges the variables cover. However, users are reminded that numerical issues may still arise; for example, in the

<sup>12</sup> <http://svo2.cab.inta-csic.es/theory/main/>

<sup>13</sup> <https://github.com/kbarbary/extinction>

<sup>14</sup> <https://www.astro.umontreal.ca/~bergeron/CoolingModels/> and <https://warwick.ac.uk/fac/sci/physics/research/astro/people/tremblay/modelgrids>

<sup>15</sup> This effect becomes even more important when the distance is a free-parameter to be fitted. But it does not lead to degeneracy because the reddening is non-linear and the effect is monotonic as a function of wavelength.

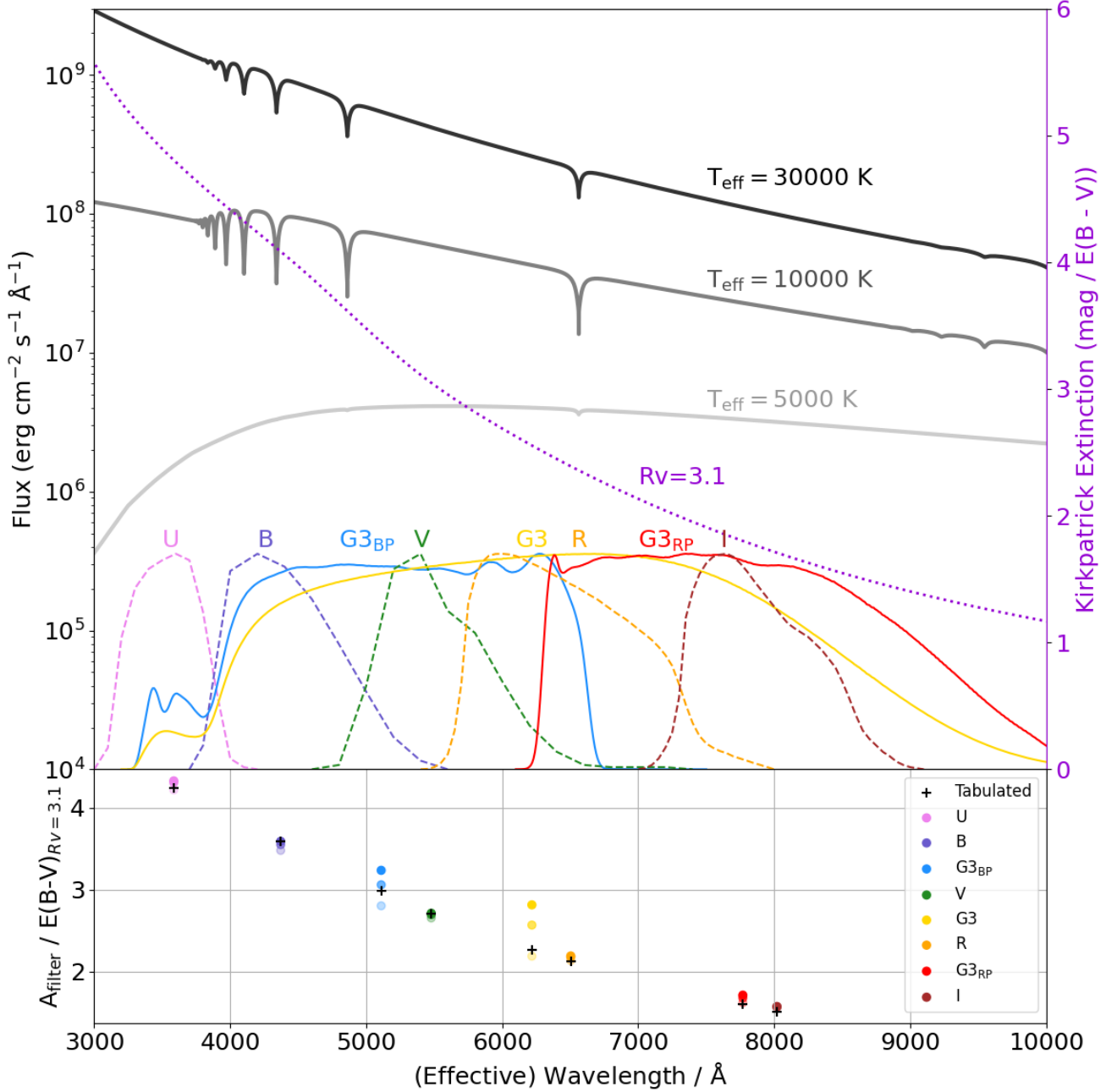


**Figure 3.** *Top:* The grey, dark-grey and black lines white dwarf spectra at  $T_{\text{eff}} = 5000$ ,  $10000$ , and  $30000$  K. The solid coloured lines (with the rainbow hue sorted by the effective wavelengths) are the filter response function. All of filters are normalised independently. The purple dotted line is the Fitzpatrick extinction law. *Bottom:* The black crosses are the pre-computed values from Schlafly & Finkbeiner (2011) using a synthetic spectrum of a  $7000$  K,  $\log(Z) = -1.0$ , and  $\log(g) = 4.5$  star. The scattered points are extinction values obtained by convolving each of the filter profiles with the extinction curve and spectra. The shade of each colour follows the same shade as the temperature shading used in the upper plot: light shade is at  $5000$  K, medium shade is at  $10000$  K and the darkest shade is at  $30000$  K. It is clear that when using Gaia filters, which are very broad, the difference in the extinction correct is non-negligible because the spectral energy distribution can vary significantly within the wavelength range of these filters.

case of a simple starburst with a duration of  $10^6$  yrs, it requires a relative error tolerance of  $10^{-10}$  in order to integrate properly for an old population.

It is also known that binary WD mergers lead to an underestimation of the age of the WDs, hence they lead to contribution of density at the “wrong magnitude” in a WDLF assumed to be attributed solely

by singly evolved WDs (Temminck et al. 2020). Another limitation is that this work does not account for the WDs escaped from clusters and have since drifted into the few-hundred-pc of the solar neighbourhood (e.g. Zuckerman et al. 2013; Heyl et al. 2022; Miller et al. 2022).

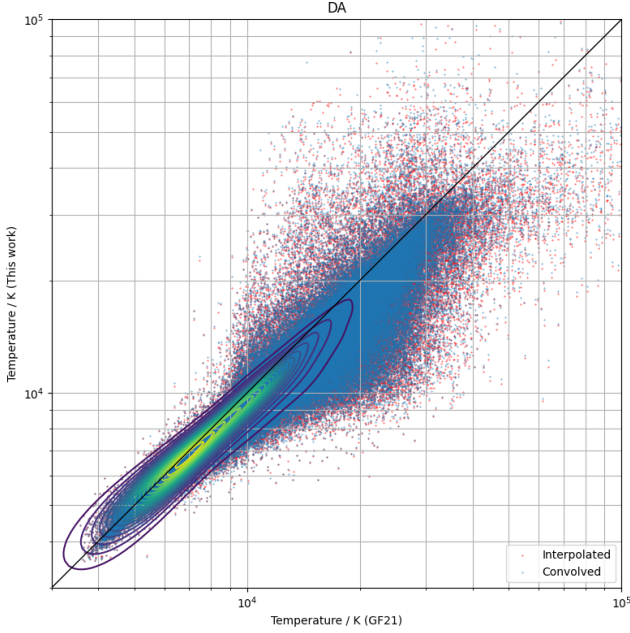


**Figure 4.** Comparison of the effective temperature fitting against GF21. The blue scattered points show all the fitted temperatures using our preferred reddening treatment adopting the interpolated reddening computed for each filter at each temperature available from the collection from Koester (2010). The red points compares when the reddening is interpolated directly using the table from Schlafly & Finkbeiner (2011) computed using a synthetic spectrum of a 7 000 K  $\log(Z) = -1$ , and  $\log(g) = 4.5$  star. The colour lines show the density of scattered points that cannot be resolved, each level of inter-contour space contains 5% of the total data. The identity line is plotted as a visual guide. The contour lines appear skewed due to the use of log-axes.

The integral for a WDLF when parameterised with bolometric magnitude ( $M_{\text{bol}}$ , as opposed to luminosity) can be written as

$$n(M_{\text{bol}}) = \int_{M_l}^{M_u} \tau(M_{\text{bol}}, M_f) \psi(T_0, M_{\text{bol}}, M_i, m, Z) \phi(M_i) dM_i \quad (9)$$

where  $n$  is the number density,  $\tau$  is the inverse cooling rate,  $\psi$  is the relative star formation rate,  $\phi$  is the initial mass function; and their dependent variables:  $M_{\text{bol}}$  is the absolute bolometric magnitude,  $M_f$  is the WD mass,  $T_0$  is the look-back time,  $M_i$  is the progenitor MS mass,  $Z$  is the metallicity,  $M_l$  is the minimum progenitor MS mass that could have singly evolved into a WD in the given time, and  $M_u$  is the maximum progenitor MS mass.

The inverse cooling rate

$$\tau(M_{\text{bol}}, M_f) = \frac{dt_{\text{cool}}}{dM_{\text{bol}}}(M_{\text{bol}}, M_f) \quad (10)$$

is a quantity taken from the pre-computed grid of cooling models.

The relative star formation rate is expressed as a function of look-back time,

$$\psi(T_0, M_{\text{bol}}, M_i, M_f, Z) = \quad (11)$$

$$\psi [T_0 - t_{\text{cool}}(M_{\text{bol}}, M_f) - t_{\text{MS}}(M_i, Z)]. \quad (12)$$

The absolute normalisation is not needed when the total stellar mass is coming from observations; the theoretical WDLF only needs to

multiply with a constant (the total number density) to account for the normalisation.

The IFMR takes a simple form of

$$M_f = \zeta(M_i), \quad (13)$$

although there is evidence that more metal-rich stars lose more envelope (Kilic et al. 2007), there is insufficient empirical data to derive an IFMR at metallicity much lower or higher than solar abundance. In the following, we will introduce the class of WDLF. Then, the physical and mathematical descriptions of five different physical inputs and their effects on a WDLF will be explained in Subsection § 5.2–5.6.

### 5.1 Class: WDLF

This class inherits from the `AtmosphereModelReader` and the `CoolingModelReader`.

A WDLF object requires seven models for computation: (1) Star Formation History (SFH), (2) Initial Mass Function (IMF), (3) Initial Final Mass Relation (IFMR), (4) total stellar evolution time model, and (5–7) low, intermediate and high mass WD cooling models. A WDLF object comes with a method to produce a diagnostic plot to inspect all the input models: the IMF, the SFH, the total stellar evolution time as a function of mass, the IFMR, and the cooling model in two formats: bolometric magnitude as a function of age, and the rate of change of the bolometric magnitude as a function of age (Figure 5 is an example of this diagnostic plot).

In the following comparisons, the default configuration uses the (1) SFH with a starburst of  $10^8$  starting at the labelled time, (2) IMF from Chabrier (2003) for single stars, (3) IFMR from Catalán et al. (2008a), and (4) cooling models from the Montreal group. While comparing the theoretical WDLFs in the following sections. We are altering one variable at a time in the comparisons.

The WDLFs in all the figures in this section are normalised at 10 mag to a log-number density of 0.0.

### 5.2 Star Formation History

WDLFs with various star formation histories are shown in Figure 6. The bright edge of the WDLFs lines up almost perfectly because WDs arrive at the corresponding bolometric magnitudes at a constant rate. The gradient is most sensitive to a time-dependent variable, for example, a change in the SFR. The sudden increase in the number density at  $M_{\text{bol}} = 14.5$  corresponds to the slow down in the cooling due to crystallisation that releases a significant amount of heat. This bump is the most prominent in the starburst profile at 6 Gyr old because WDs with  $\sim 0.8 - 1.0 M_{\odot}$  have the lowest cooling rates, they correspond to  $3 - 5 M_{\odot}$  ZAMS mass that spends 0.1 – 0.5 Gyr in the MS and 5 – 6 Gyr to reach 14.5 mag ( $\sim 5500$  K, Bergeron et al. 2019). The detailed description of the shape of the WDLFs due to various cooling mechanisms should be referred to Figure 5 and Section 3 of Fontaine et al. 2001. These WDLFs are only served to demonstrate the effect of SFH on their shapes, they illustrate that the faint end of a WDLF is the most important and sensitive in revealing the past star formation history of a stellar population.

The SFH has one of the strongest effects on the shape and normalisation of a WDLF. We only provide three types of simple form SFH profiles. All of them are controlled by a few simple parameters, and the fourth option is to provide a callable function of star formation rate as a function of lookback time: (1) *Constant* profile depends only on the age of the population, i.e. the lookback time since the beginning of star formation, and **not** the time since the



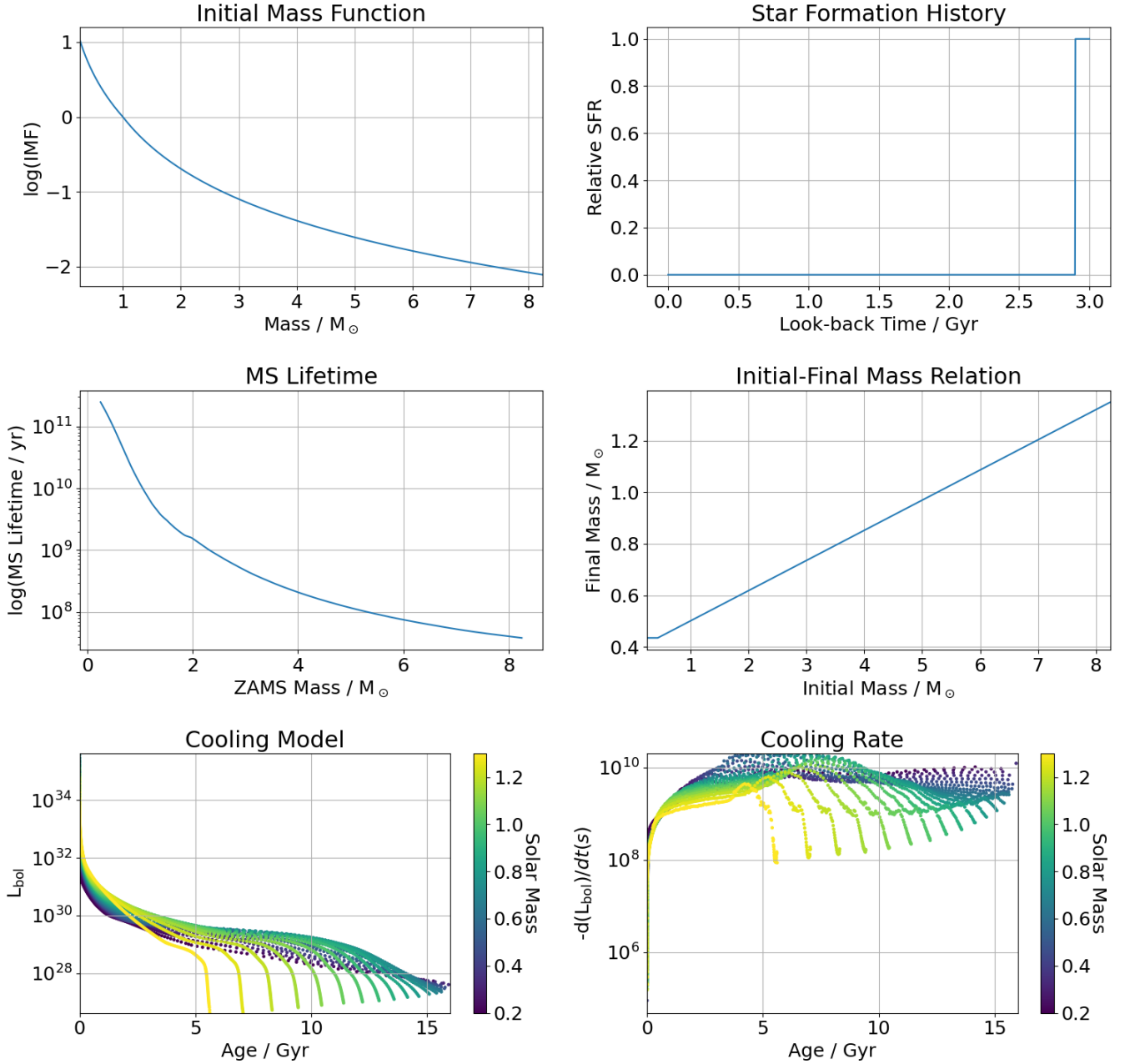


**Figure 5.** Top left: Input initial mass function. Top right: Input star formation history. Middle left: Input MS lifetime model. Middle right: Input IFMR model. Bottom left: Input cooling model showing the absolute bolometric magnitude as a function of mass and age. Bottom right: Input cooling model showing the rate of change of bolometric magnitude as a function of mass and age.

first WD was formed. (2) *Burst* profile which depends on the onset of star formation as well as the duration of a constant burst of star formation. It would be useful for studying open or globular clusters (3) An *exponentially decaying* profile that is governed by the onset of star formation, the decay coefficient and the duration of the star formation. It should give a first good guess for a disk population. By default, it continues to decay indefinitely. (4) A *manually provided callable function* that can take any form, though users should be careful with the extrapolation setting, a smoothly extrapolated value or

zero should be returned. In the case of NaN or  $\pm\text{inf}$  being returned, we set the value to zero.

This is by far the single most important time-dependent variable when computing a WDLF. Deriving the SFH from a WDLF is one of the most important reasons we are interested in computing them in the first place. It was proven to successfully mathematically invert a WDLF to retrieve the SFH of the solar neighbourhood (Rowell 2013) with the SDSS and SuperCOSMOS WDLFs (Holberg & Bergeron 2006; Rowell & Hambly 2011).

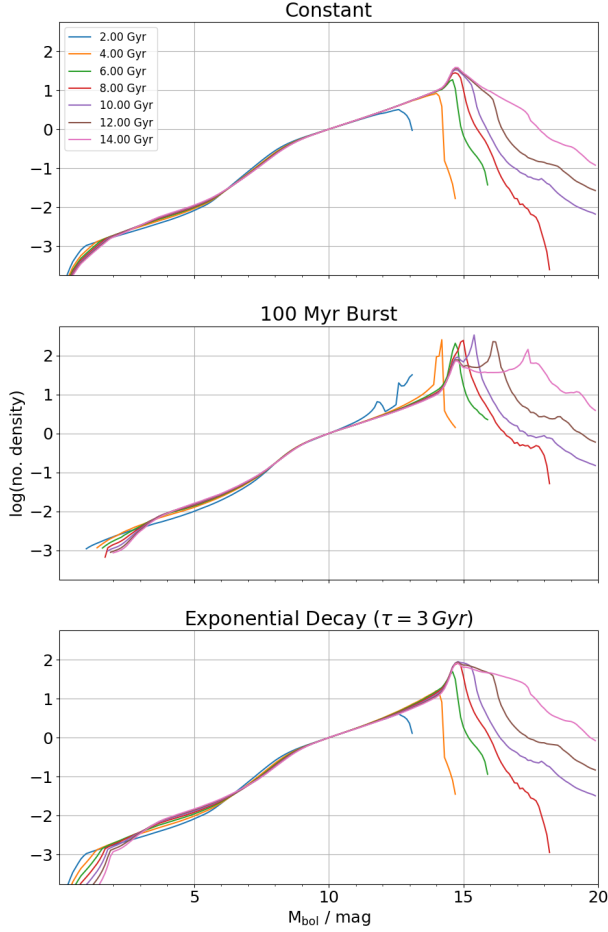


**Figure 6.** Comparing WDLFs with the three default types of star formation history from 2 to 14 Gyr in increment of 2 Gyr. Top: constant star formation since the labelled lookback time. Middle: a starburst in the first 100 Myr since the labelled lookback time. Bottom: an exponentially decaying star formation rate with a decay constant of 3 Gyr since the labelled lookback time.

Since we normalise the output WDLF by the total integrated number density at all luminosities, the absolute normalisation of the input SFH is discarded when provided manually.

### 5.3 Initial Mass Function (IMF)

The choice of any of the three built-in Galactic IMFs has little effect on the shape of the WDLF because they are identical above  $1 M_{\odot}$ . They only diverge slightly when the mass is below that  $1 M_{\odot}$ . This effect can appear in the bright end of a WDLF for old populations when the low mass stars start becoming WDs (See Figure 7 and 8). Apart from the three built-in IMF functions, a callable function can be supplied as a manual IMF. For example, if a user would like to explore the effect of a top heavy IMF, they would have to provide it manually. This lists the four options that are available:

- (i) K01: [Kroupa \(2001\)](#) is a three-part power law that only the more massive two are of relevance to this work, with  $\xi(M_i) = M_i^{-\alpha}$

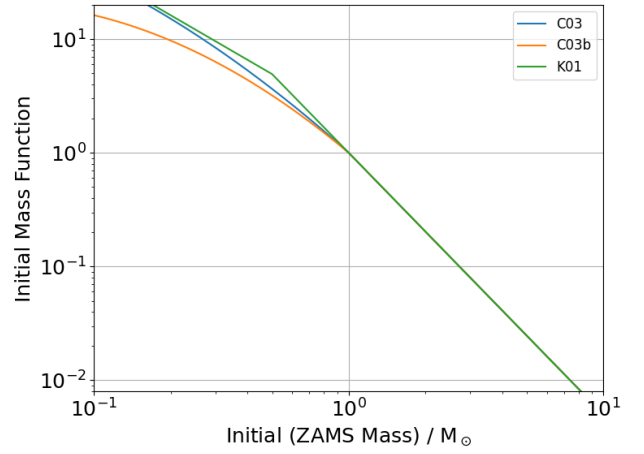


**Figure 7.** Comparing the three IMFs provided in this package. They are identical in the mass range above  $1 M_{\odot}$ , while under this mass limit, the differences are small in the mass range ( $\gtrsim 0.9 M_{\odot}$ ) that is relevant to singly evolved MS that had enough time to evolve into a WD given the finite age of the Universe.

where

$$\alpha = \begin{cases} 0.3, & M_i \leq 0.08 M_{\odot} \\ 1.3, & 0.08 \leq M_i \leq 0.5 M_{\odot} \\ 2.3, & M_i \geq 0.5 M_{\odot}. \end{cases} \quad (14)$$

- (ii) C03: [Chabrier \(2003\)](#) shares the same power law with [Kroupa \(2001\)](#) for mass above  $1 M_{\odot}$ , while below that, the IMF follows a log-normal form with

$$\xi(M_i) = \frac{0.158^{+0.051}_{-0.046}}{M_i \ln(10)} \times \exp \left\{ \frac{\left[ \log_{10}(M_i) - \log_{10} \left( 0.079^{+0.016}_{-0.021} \right) \right]^2}{2 \times (0.69^{+0.01}_{-0.05})^2} \right\} \quad (15)$$

- (iii) C03b: [Chabrier \(2003\)](#), including binary) also consider the correction for binaries which gives a much shallower IMF at the low mass end

$$\xi(M_i) = \frac{0.086}{M_i \ln(10)} \times \exp \left\{ \frac{\left[ \log_{10}(M_i) - \log_{10} (0.022) \right]^2}{2 \times (0.57)^2} \right\} \quad (16)$$

- (iv) Manually provide an interpolated function that returns the initial mass density as a list or an array (even if a single point is returned).

There is a very weak dependency on the IMF because the three IMFs are only different at mass below  $1 M_{\odot}$ , which has an MS lifetime of  $\sim 11$  Gyr for solar metallicity stars. Hence, we only start to see a difference in the WDLF at ages above 11 Gyr (Figure 8). The IMFs only diverge significantly well into the M-dwarf/brown dwarf regime. Even at a computed age of 15 Gyr we are only including stars with ZAM masses as low as  $\sim 0.96 M_{\odot}$ . Nevertheless, if a metal-poor MS lifetime model is used, this can change the picture slightly as they are more short-lived.

### 5.4 Initial-Final Mass Relations

In Fig. 9, the WDLFs in the range of 9–14 mag line up almost perfectly at any age. This is because WDs with a ‘typical mass’ do not

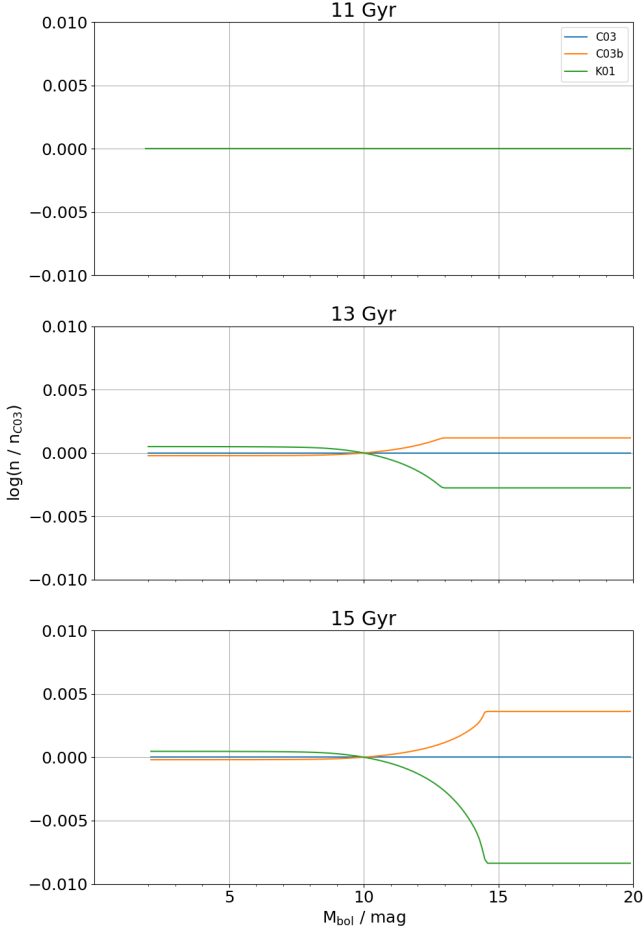


**Figure 8.** The initial mass functions are identical above  $1 M_{\odot}$ , only the oldest populations show differences in the bright end of the WDLFs. Due to almost identical computed WDLFs, only the differences of the WDLFs relative to the C03 are shown.

have strong mass-dependent physical phenomenon that affects the WD evolution. They all cool at roughly the same rate across the mass range of the models. However, the difference is still measurable and obvious by eye when the systems have sufficient time to evolve and for the WDs to cool. In Figure 9, the 5 Gyr comparison plot is exhibiting the dip in the EB18 IFMR just above  $5 M_{\odot}$  at 14.5 mag. Meanwhile the strong feature at 14.0–14.5 mag in S09 (red), K09 (brown), K09b (pink), and C18 (grey) are when the respective IFMRs are crossing the C09 IFMR from a higher final mass than C08’s to a lower final mass. Such an effect can be seen propagating down the WDLFs from the younger populations to the older at about 1 mag every 2 Gyr. Similarly, in the oldest system, we can see that when  $0.9 M_{\odot}$  have recently become WDs in the 13 and 15 Gyr, only the S09b (red) and W09 (purple) models that return lower WD mass than that from C08 are showing deficiencies at the brightest end.

The comparison in Figure 9 reaffirms the finding from Catalán et al. (2008a) that the choice of IFMR has little effect on the shape of the WDLFs at  $M_{\text{bol}} > 4$ . We have also shown in the figure that the peaks of the WDLFs differ slightly in the bolometric magnitude at a given age. That comes from the accumulation of a slightly different cooling rate over a cosmic time when a progenitor at a given mass

turns into slightly different mass WDs as prescribed by the different IFMRs.

Human civilisation has existed for a mere few thousand years, and modern astronomy (with digital aid) for no more than a hundred. We do not have direct observations on the total mass loss of a star at the end stage of stellar evolution. It depends on observations of WDs and giants in clusters and iteratively comparing with stellar evolution models. There are a number of IFMRs available from studying globular clusters (Moehler et al. 2004; Kalirai et al. 2009), open clusters (Williams et al. 2009; Cummings et al. 2016), a mix of globular and open cluster (Cummings et al. 2018), wide MS-WD binaries (Catalán et al. 2008b; Zhao et al. 2012), wide turnoff/subgiant-WD binaries (Barrientos & Chanamé 2021), wide WD-WD binaries (Catalán 2015; Andrews et al. 2015), and colour-magnitude diagram fitting (El-Badry et al. 2018). We have chosen six (plus three with two-part fitting) works that have a good mass coverage to be included in this work, and just like the other functions above, a manually provided callable function is also accepted:

(i) C08: Catalán et al. (2008a) – this work reanalysed all the known WDs in clusters and MS-WD binaries homogeneously by using a single stellar evolution model and a single WD cooling model. The sample covers a mass range of  $1.5 - 6.4 M_{\odot}$ , giving a best-fit IFMR of

$$M_f = (0.117 \pm 0.004) M_i + (0.384 \pm 0.011) M_{\odot}. \quad (17)$$

(ii) C08b: Catalán et al. (2008a, two-part) – in the same work, they also fitted with a 2-part IFMR with a breakpoint at  $2.7 M_{\odot}$ , which gives a steeper relation at the high mass end with

$$M_f = \begin{cases} (0.096 \pm 0.005) M_i + (0.429 \pm 0.015) M_{\odot}, & (M_i \leq 2.7 M_{\odot}) \\ (0.137 \pm 0.007) M_i + (0.318 \pm 0.018) M_{\odot}, & (M_i \geq 2.7 M_{\odot}) \end{cases} \quad (18)$$

(iii) S09: Salaris et al. (2009) – by using 10 (young) open clusters, this relation is probing the high mass end of the population that can turn into WDs. They, however, do not have enough time for the lower mass stars to evolve into WDs hence this relation is unconstrained below  $1.7 M_{\odot}$  and we extrapolate if the given initial mass is below  $1.7 M_{\odot}$ . The upper limit of the data set is  $8.5 M_{\odot}$ :

$$M_f = 0.084 M_i \pm 0.466 M_{\odot}. \quad (19)$$

(iv) S09b: Salaris et al. (2009, two-part) – in the same work, they also fitted with a 2-part IFMR with a break point at  $4 M_{\odot}$ .

$$M_f = \begin{cases} 0.134 M_i + 0.331 M_{\odot}, & 1.7 M_{\odot} \leq M_i \leq 4.0 M_{\odot} \\ 0.047 M_i + 0.679 M_{\odot}, & M_i \geq 4.0 M_{\odot} \end{cases} \quad (20)$$

(v) W09: Williams et al. (2009) is an extension to Salaris et al. (2009) by including M41 to the collection of open clusters, covering a reliable mass range of  $1.25 - 8.0 M_{\odot}$ ,

$$M_f = (0.129 \pm 0.004) M_i + (0.339 \pm 0.015) M_{\odot}. \quad (21)$$

(vi) K09: Kalirai et al. (2009) reanalysed with all the available open clusters covering a mass range of  $1.1 - 6.5 M_{\odot}$  to give a relation of

$$M_f = (0.109 \pm 0.007) M_i + (0.428 \pm 0.025) M_{\odot}. \quad (22)$$

(vii) K09b: Kalirai et al. (2009, extended) includes also the WDs from the globular cluster, M4, to give a shallower relation.

$$M_f = (0.101 \pm 0.006) M_i + (0.463 \pm 0.018) M_{\odot}. \quad (23)$$

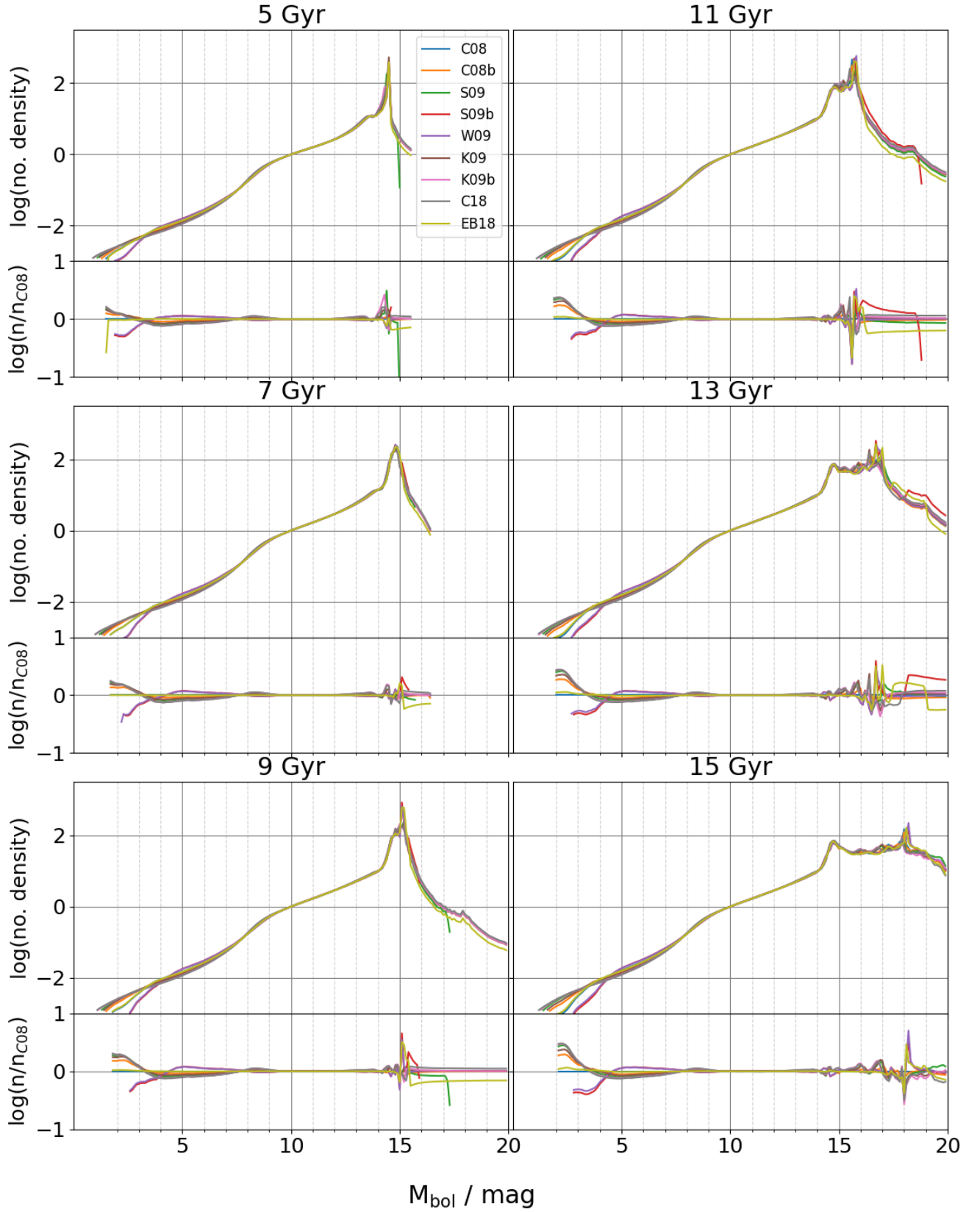


**Figure 9.** Comparing WDLFs with different input IFMRs. Its effect on the WDLF is small because of the similarity between them. The large difference at the bright end is due to the relatively large difference in the cooling rate among the new hot WDs. The differences in the faint end come from the accumulation of different cooling rates at slightly different WD masses for a progenitor at a given mass.



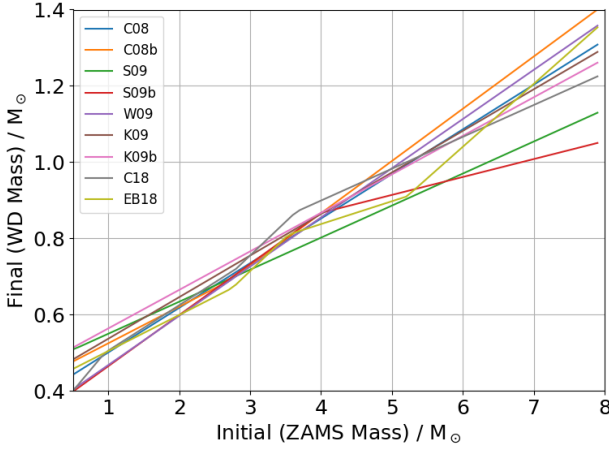


**Figure 10.** Comparing the three IFMRs provided in this package. They follow a similar trend and they are mostly lying on top of each other. S09 and S09b have the shallowest IFMRs at the massive end of the initial mass among all. However, given the steep decline of the initial mass function,  $7 M_{\odot}$  MS stars are about 10 times less common than  $3 M_{\odot}$  MS stars and about 100 times less common than  $1 M_{\odot}$  MS stars. Hence, the discrepancy also only attribute to a small effect in the final WDLFs (See Figure 9)

However, having only metal richer open cluster data at the high mass end and only the metal-poor globular cluster data at the low mass end is likely to lead to a shallower fit expected due to the metallicity dependency in the total mass loss at the late stage of stellar evolution.

(viii) C18: Cummings et al. (2018) has fitted and compared various theoretical and empirical models, we are only providing the 3-part-solution that the authors preferred, which is based on the MIST stellar evolution model,

$$M_f = \begin{cases} (0.080 \pm 0.016) M_i + (0.489 \pm 0.030) M_{\odot}, & (0.83 M_{\odot} \leq M_i \leq 2.85 M_{\odot}) \\ (0.187 \pm 0.061) M_i + (0.184 \pm 0.199) M_{\odot}, & (2.85 M_{\odot} \leq M_i \leq 3.6 M_{\odot}) \\ (0.107 \pm 0.016) M_i + (0.471 \pm 0.077) M_{\odot}, & (3.6 M_{\odot} \leq M_i \leq 7.2 M_{\odot}) \end{cases} \quad (24)$$

(ix) EB18: El-Badry et al. (2018) reports the relations by fitting the colour-magnitude diagram of the clean Gaia DR2 WD sequence. It is a 5-point piecewise-linear function going through the following (initial mass, final mass) coordinates:  $(0.95, 0.5^{+0.01}_{-0.01})$ ,  $(2.75^{+0.36}_{-0.31}, 0.67^{+0.02}_{-0.02})$ ,  $(3.54^{+0.55}_{-0.43}, 0.81^{+0.03}_{-0.03})$ ,  $(5.21^{+1.06}_{-0.71}, 0.91^{+0.10}_{-0.03})$  and  $(8.0, 1.37^{+0.06}_{-0.21})$ .

(x) Manually provided an interpolated function that returns the final mass as a list or an array (even if a single point is returned).

## 5.5 Total Stellar Evolution Time

The effect of metallicity on the WDLF is qualitatively described as follows: the more massive stars become WDs at roughly the same time, so the faint end of the WDLFs show little differences. However, the evolution times for the lower mass stars reduce with metallicity. Thus, at the bright end of a WDLF which is dominated by low mass stars, using a low metallicity stellar evolution model would ‘squeeze’ the WDLF towards its fainter part, giving a WDLF with

a steeper gradient on the bright side. This makes a system appears older if a low metallicity model is used for interpreting a more metal-rich population, and vice versa. This effect should be considered in conjunction with the metallicity dependence of the IFMR in the future when such a relation becomes better constrained.

The total stellar evolution lifetime has a strong effect on the bright end of a WDLF because the hot WDs spent most of their time since star formation as their progenitors. However, the MS lifetime has decreasing impact on the WDLF as we move towards the fainter end where WDs cooling time dominates over the MS lifetime. There is also a metallicity dependency on the MS lifetime. From the PARSEC models (Bressan et al. 2013), an extremely metal poor  $1 M_{\odot}$  star with  $Z = 0.0001$  and a solar-metallicity star with  $Z = 0.017$  take  $\sim 6$  Gyr and  $\sim 11$  Gyr to go through the stellar evolution stages, respectively, before becoming a WD. In the WDPHOTools, we provide 15 models from PARSEC (Bressan et al. 2012, 2013; Chen et al. 2014), 3 from the Geneva Code (Ekström et al. 2012; Mowlavi et al. 2012; Georgy et al. 2013a,b), and 15 from the MIST (Paxton et al. 2011, 2013, 2015; Dotter 2016; Choi et al. 2016). The following stellar evolution lifetime models are interpolated and the option of providing a callable function is also a possible form as input:

- (i) PARSECz00001 ( $Z = 0.0001$ ,  $Y = 0.249$ )
- (ii) PARSECz00002 ( $Z = 0.0002$ ,  $Y = 0.249$ )
- (iii) PARSECz00005 ( $Z = 0.0005$ ,  $Y = 0.249$ )
- (iv) PARSECz0001 ( $Z = 0.001$ ,  $Y = 0.25$ )
- (v) PARSECz0002 ( $Z = 0.002$ ,  $Y = 0.252$ )
- (vi) PARSECz0004 ( $Z = 0.004$ ,  $Y = 0.256$ )
- (vii) PARSECz0006 ( $Z = 0.006$ ,  $Y = 0.259$ )
- (viii) PARSECz0008 ( $Z = 0.008$ ,  $Y = 0.263$ )
- (ix) PARSECz001 ( $Z = 0.01$ ,  $Y = 0.267$ )
- (x) PARSECz0014 ( $Z = 0.014$ ,  $Y = 0.273$ )
- (xi) PARSECz0017 ( $Z = 0.017$ ,  $Y = 0.279$ )
- (xii) PARSECz002 ( $Z = 0.02$ ,  $Y = 0.284$ )
- (xiii) PARSECz003 ( $Z = 0.03$ ,  $Y = 0.302$ )
- (xiv) PARSECz004 ( $Z = 0.04$ ,  $Y = 0.321$ )
- (xv) PARSECz006 ( $Z = 0.06$ ,  $Y = 0.356$ )
- (xvi) GENEVAz002 ( $Z = 0.002$ )
- (xvii) GENEVAz006 ( $Z = 0.006$ )
- (xviii) GENEVAz014 ( $Z = 0.014$ )
- (xix) MISTFem400 ( $[\text{Fe}/\text{H}] = -4.0$ )
- (xx) MISTFem350 ( $[\text{Fe}/\text{H}] = -3.5$ )
- (xxi) MISTFem300 ( $[\text{Fe}/\text{H}] = -3.0$ )
- (xxii) MISTFem250 ( $[\text{Fe}/\text{H}] = -2.5$ )
- (xxiii) MISTFem200 ( $[\text{Fe}/\text{H}] = -2.0$ )
- (xxiv) MISTFem175 ( $[\text{Fe}/\text{H}] = -1.75$ )
- (xxv) MISTFem150 ( $[\text{Fe}/\text{H}] = -1.5$ )
- (xxvi) MISTFem125 ( $[\text{Fe}/\text{H}] = -1.25$ )
- (xxvii) MISTFem100 ( $[\text{Fe}/\text{H}] = -1.0$ )
- (xxviii) MISTFem075 ( $[\text{Fe}/\text{H}] = -0.75$ )
- (xxix) MISTFem050 ( $[\text{Fe}/\text{H}] = -0.5$ )
- (xxx) MISTFem025 ( $[\text{Fe}/\text{H}] = -0.25$ )
- (xxxi) MISTFe000 ( $[\text{Fe}/\text{H}] = 0.0$ )
- (xxxii) MISTFe025 ( $[\text{Fe}/\text{H}] = 0.25$ )
- (xxxiii) MISTFe050 ( $[\text{Fe}/\text{H}] = 0.5$ )
- (xxxiv) Manual

A few models are plotted in Fig. 11 to illustrate the differences in the MS lifetime at difference masses and metallicities.

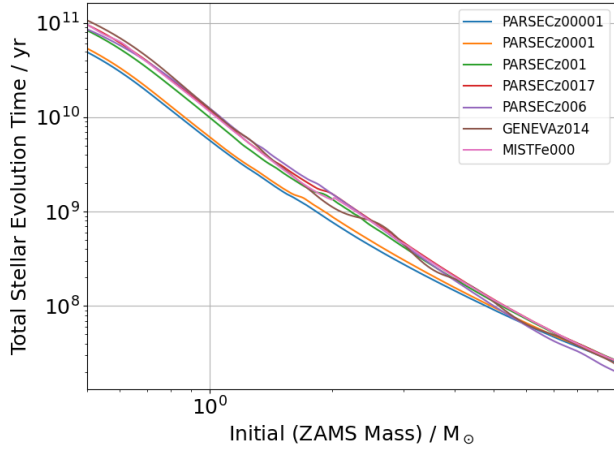


**Figure 11.** Comparing seven of the 33 available models: PARSEC is shown with metallicity at  $z = 0.0001, 0.001, 0.01, 0.017$  (i.e. solar) and 0.06; Geneva and MIST solar metallicity model is plotted for comparison. The low metallicity stars evolve more quickly than their higher metallicity counterparts. At 1 solar mass, the most metal-poor model evolves twice as fast as the solar metallicity one. At higher mass, the discrepancy is smaller at different metallicity and from different models.

## 5.6 Cooling Models

Most of the internal energy of a WD is the residual heat from the progenitor once it passed the planetary nebula phase. However, there are various physical processes that can provide an appreciable amount of energy and govern the cooling rate of a WD at different stages. Following the time sequence in which the physical processes that have direct effects on the photo-luminosity:

- (i) in the first  $10^8 - 10^9$  years, *shell burning of hydrogen* via pp-chain can contribute up to 30% of the total luminosity (Renedo et al. 2010).
- (ii) *Neutrino losses* – contribute to a significant fraction of energy loss in the early time of WDs when they were still hot, in the case of massive WDs, neutrino bremsstrahlung effect must also be taken into account (Haft et al. 1994; Itoh et al. 1996).
- (iii) *Gravitational settling* of  $^{22}\text{Ne}$  in intermediate to massive WDs releases sufficient gravitational potential energy to prolong the cooling times (Deloye & Bildsten 2002; García-Berro et al. 2008; Althaus et al. 2010b). The heavier  $^{22}\text{Ne}$  relative to the environment that is dominated by carbon, oxygen and nitrogen leads to a slow settling towards the core. This effect is the most obvious in the old and metal-rich systems, such as NGC 6791 (García-Berro et al. 2010; Bedin et al. 2008).
- (iv) In the late time of the WD evolution, convection plays a significant role in slowing down the cooling. As temperature decreases, the convective zone grows deeper into the interior and eventually reaches the degenerate core (see Figure 11 from Althaus et al. 2010a). This efficiently replenishes the energy radiated away from the photosphere, thus this process known as the *convective coupling*, modifies the relations between the WD luminosity and core temperature (D’Antona & Mazzitelli 1989; Fontaine et al. 2001).
- (v) *Crystallisation* occurs as the non-degenerate ions evolve from gas to fluid and eventually solid. The liquid-solid transition releases latent heat that slows down the cooling process. This also couples with the release of gravitational energy associated with changes in the

carbon-oxygen profile (Salaris et al. 1997) when the heavier oxygen-rich crystals displace carbon as a result of gravitational settling.

(vi) Depending on the changes in the carbon-oxygen abundance profile, and the choice of phase diagram of a carbon-oxygen mixture, it modifies the rate of cooling and this specific effect is colloquially known as the *Phase Separation* effect.

(vii) *Coulomb Interactions* modify the thermodynamical properties of the ionic gas, in particular the specific heat. Its strength is determined by the Coulomb coupling parameters. At first, the parameter is small, it slowly increases as a WD cools and the ions begin to change from gas to liquid and eventually form lattice. This releases latent heat that contributes to  $\sim 5\%$  of the total luminosity (Shaviv & Kovetz 1976). At late time, a few modes of the lattice are excited, the heat capacity drops according to the Debye law, which results in enhanced cooling. This process kicks in after  $10^9$  yr for a  $1.0 M_\odot$  WD, and after more than a Hubble time for a  $0.5 M_\odot$  WD.

We have included 24 cooling models from sixteen pieces of work that cover different parts of the parameter space. The following lists the keywords for choosing the models:

- (i) montreal\_co\_da\_20 (Bédard et al. 2020)
- (ii) montreal\_co\_db\_20 (Bédard et al. 2020)
- (iii) lpcode\_he\_da\_07 (Panei et al. 2007)
- (iv) lpcode\_he\_da\_09 (Althaus et al. 2009)
- (v) lpcode\_co\_da\_07 (Panei et al. 2007)
- (vi) lpcode\_co\_da\_10\_z001 (Renedo et al. 2010)
- (vii) lpcode\_co\_da\_10\_z0001 (Renedo et al. 2010)
- (viii) lpcode\_co\_da\_15\_z00003 (Althaus et al. 2015)
- (ix) lpcode\_co\_da\_15\_z0001 (Althaus et al. 2015)
- (x) lpcode\_co\_da\_15\_z0005 (Althaus et al. 2015)
- (xi) lpcode\_co\_db\_17\_z00005 (Althaus et al. 2017)
- (xii) lpcode\_co\_db\_17\_z0001 (Althaus et al. 2017)
- (xiii) lpcode\_co\_db\_17 (Camisassa et al. 2017)
- (xiv) lpcode\_one\_da\_07 (Althaus et al. 2007)
- (xv) lpcode\_one\_da\_19 (Camisassa et al. 2019)
- (xvi) lpcode\_one\_db\_19 (Camisassa et al. 2019)
- (xvii) lpcode\_da\_22 (Althaus et al. 2013; Camisassa et al. 2016, 2019)
- (xviii) lpcode\_db\_22 (Camisassa et al. 2017, 2019)
- (xix) basti\_co\_da\_10 (Salaris et al. 2010)
- (xx) basti\_co\_db\_10 (Salaris et al. 2010)
- (xxi) basti\_co\_da\_10\_nps (Salaris et al. 2010)
- (xxii) basti\_co\_db\_10\_nps (Salaris et al. 2010)
- (xxiii) mesa\_one\_da\_18 (Lauffer et al. 2018)
- (xxiv) mesa\_one\_db\_18 (Lauffer et al. 2018)

See Table 1 for the details of each model. We divide the models into three groups: low ( $M/M_\odot < 0.5$ ), intermediate ( $0.5 < M/M_\odot < 1.0$ ) and high mass ( $M/M_\odot > 1.0$ ). For the lowest mass one, it is only used in the cases where the IFMR gives WDs reaching such mass, and a population that can be old enough to produce these low mass singly evolved WDs.

There are too many possible combinations of cooling models to display them all, so in Figure 12, only four example sets of models are shown. The combinations are listed in Table 2. In order to assess the quality of the interpolation at the model boundaries at the three mass ranges, we can compute the total WDLF by summing the constituent low, intermediate and high mass WDLFs by setting two of three models to None each time, and then compared it to a WDLF computed using a single interpolated grid across all three mass ranges.

In combination A, we use the pure Montreal stack. This naturally gives the smoothest interpolated grid across the entire parameter

Reference	Low	Intermediate	High	Core	Atmosphere	Mass Range ( $M_f / M_\odot$ )	Extra Notes
Montreal smooth grid							
Bédard et al. (2020, B20)	✓	✓	✓	CO	H/He	0.2 – 1.3	–
BaSTI smooth grid							
Salaris et al. (2010, S10)	–	✓	✓	CO	H/He	0.54 – 1.2	W/Wo <sup>†</sup> Phase Separation
LPCODE smooth grid							
Althaus et al. (2013)	✓	–	–	He	H	–	–
Camisassa et al. (2016)	–	✓	–	He	H	–	–
Camisassa et al. (2019)	–	–	✓	He	H	–	–
Camisassa et al. (2017)	–	✓	–	He	He	–	–
Camisassa et al. (2019)	–	–	✓	He	He	–	–
LPCODE							
Panei et al. (2007)	✓	–	–	He/CO	H	0.187 – 0.448	–
Althaus et al. (2009, A09)	✓	–	–	He	H	0.220 – 0.521	–
Renedo et al. (2010, R10)	–	✓	–	CO	H	0.505 – 0.934	$Z = 0.001 – 0.01$
Althaus et al. (2015)	–	✓	–	CO	H	0.506 – 0.826	$Z = 0.0003 – 0.001$
Althaus et al. (2017)	✓	✓	–	CO	H	0.434 – 0.838	$Y = 0.4$
Camisassa et al. (2017)	–	✓	–	CO	He	0.51 – 1.0	–
Althaus et al. (2007)	–	–	✓	ONe	He	1.06 – 1.28	–
Camisassa et al. (2019, C19)	–	–	✓	ONe	H/He	1.10 – 1.29	–
MESA-based Models							
Lauffer et al. (2018)	–	–	✓	CO/Ne	H/He	1.012 – 1.308	–

**Table 1.** The complete listing of all the cooling models available from the public domain contained in WDPHOTTOOLS. They broadly come from four sources, where the LPCODE has the most varied grid for various parameters. The three *smooth grids* can provide the smoothest interpolated cooling models, the mix-and-match of other models are likely to produce artefacts. We recommend separating the low, intermediate and high mass models to generate subset of the WDLFs and add their contribution together to achieve better solutions.

The checkmarks in the low ( $M_f / M_\odot < 0.5$ ), intermediate ( $0.5 < M_f / M_\odot < 1.0$ ) and high mass ( $1.0 < M_f / M_\odot$ ) ranges denotes if the models are used for computation in that range. (<sup>†</sup> *With/Without.*)

Combination	Low Mass	Intermediate Mass	High Mass
A	B20	B20	B20
B	A09	R10	C19
C	B20	S10	S10
D	B20	S10 (nps)	S10 (nps)

**Table 2.** Combination of the models used to compare the output WDLFs (Refer to Table 1 for the model names and properties).

space because of the homogeneous choice of input physics and computation tools. Combination B makes use of the most recent low, intermediate and high mass models from the LPCODE<sup>16</sup>. In combinations C and D, the low mass model is adopting that from the Montreal group, while the intermediate and high mass models are from the BaSTI with and without the inclusion of phase separation in the computation.

In B and C, the lump at the faintest end is due to the choice of ONe WDs for  $> 1 M_\odot$  WDs. They have different thermal properties to CO WDs so they do not accumulate at the same bolometric magnitudes as the CO WDs when cooling down.

<sup>16</sup> We use the smooth grid pre-interpolated by their research group, as opposed to the individually published grids.

## 6 OTHER UTILITIES

There are two modules used in the background, `reddening` and `util`; and one module, `plotter`, that could be useful for basic inspection of the models.

The `reddening` handles either choice of interpolation of the extinctions, using a customised 2D spline interpolator if the tabulated values from [Schlafly & Finkbeiner \(2011\)](#) is used; or with the `scipy.interpolate.RegularGridInterpolator` if the spectral type corrected extinction values are chosen for dereddening. As mentioned in Section 4.5, the extinction coefficient is tailored to the temperature and the surface gravity of the target. Those coefficients are obtained by convolving filter profiles with model spectra and convert the total extinction into the extinction in each filter as a function of temperature and surface gravity.

The other background module, `util`, supplies the customised 2D spline. Figure 1 is the default plot making use of the `plotter` for displaying the Montreal atmosphere model. Similar plots can be generated for inspecting the cooling models.

## 7 SUMMARY AND FUTURE PLAN

We provide a toolkit to allow easy access to synthetic photometry of WDs with a number of formatters to handle the non-uniform model files and units from various models. These models can be flexibly interpolated with two choices of interpolators for immediate use with

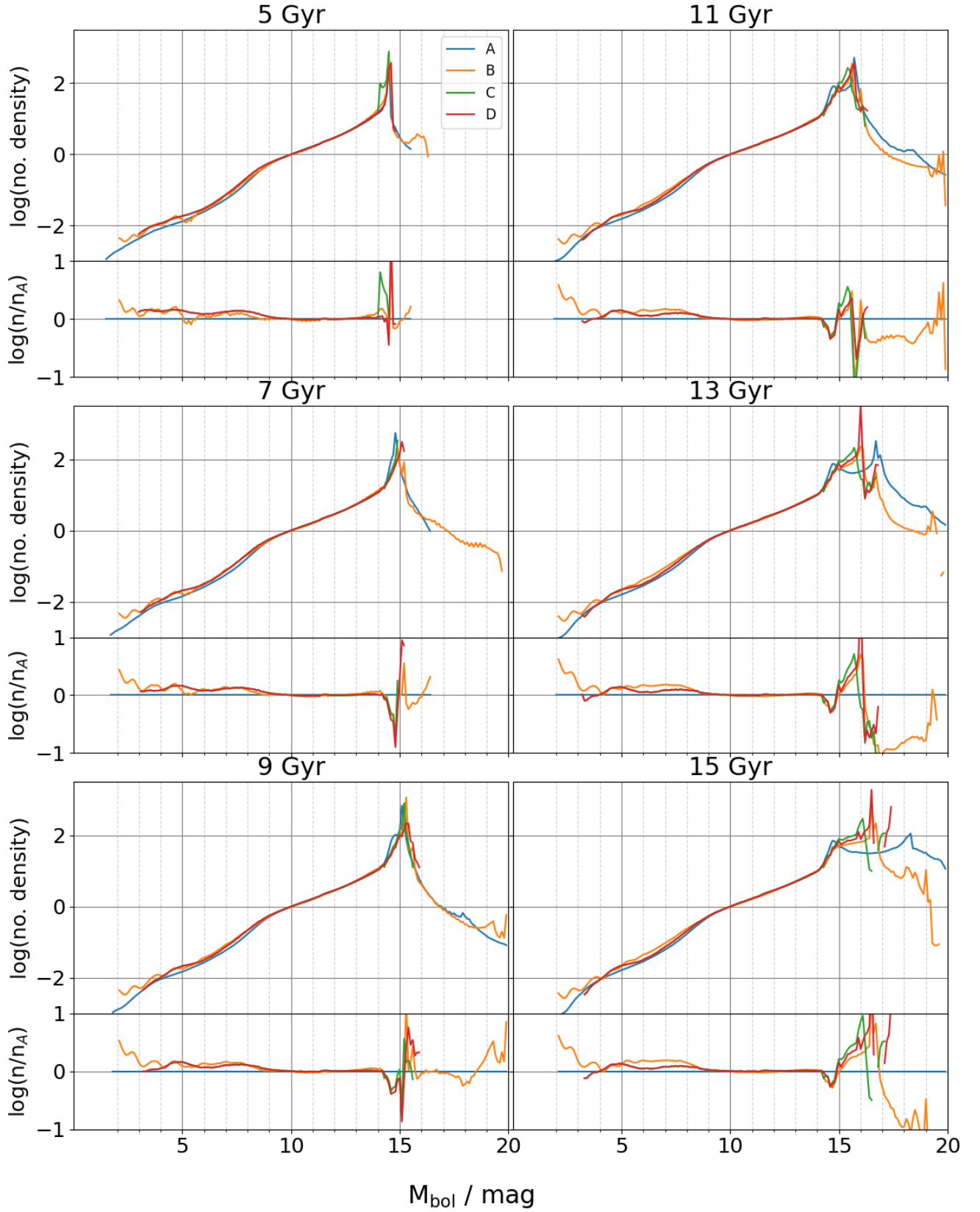


**Figure 12.** Comparing WDLFs with different input cooling models. See Table 2 for the choice of input models. The differences in the WDLFs are small down to 14 mag. After that, the input Physics in handling gravitational settling of heavy elements, convective coupling, crystallisation, phase separation, and Coulomb interactions vary and are setting in at different times (see Section 5.6 for more details).



ease. Building on these interpolated grids, this toolkit can perform photometric fitting of WDs with or without a known distance, though the reliability is much higher if the distance is provided, and it can also correct for reddening at each step of the iteration during the minimisation/sampling.

We also make sure this grid provides a convenient and flexible tool to construct WDLFs, allowing users to choose from a large number of stellar evolution models and cooling models. We cover one set of DA and DB atmosphere model, three initial mass functions, and three preset star formation history models (constant, exponentially decay and burst). User-defined input models can be supplied for each step of the WDLF computation (apart from the cooling model), in order to allow a high level of flexibility when it comes to more advanced usage.

In the future development of WDPHOTTOOLS, we intend to

- (i) include new models that will become available;
- (ii) include synthetic photometry also provided in some of the cooling models;
- (iii) include means to use a user provided filter profile that can be convolved with the spectral energy distribution functions publicly available<sup>17</sup>;
- (iv) allow the use of different mass-radius relations;
- (v) use user provided interstellar extinction correction;
- (vi) user supplied interpolator.

In the coming decades, we shall expect higher quality distance estimates from the future Gaia data releases, and deeper photometry couple with proper motion measurements (an alternative way to effectively select WD) with the new generation facilities, for example, the Vera Rubin Observatory for the southern sky, EUCLID and the Nancy Grace Roman Telescope for the study of the halo WDs (Fantin et al. 2020). The WDPHOTTOOLS will provide a user-friendly, convenient, and flexible tool for this generation of astronomers to have an easier starting position and a more gentle initial learning curve.

## ACKNOWLEDGEMENTS

The authors thank the anonymous referees for their comments that significantly improve the readability of the articles.

MCL and MJG are supported by a European Research Council (ERC) grant under the European Union’s Horizon 2020 research and innovation program (grant agreement number 833031).

MCL thanks Dr. N. Hambly and Dr. N. Rowell for their supports and guidance over the years, as well as Dr. R. Smith, Prof Ł Wyrzykowski, Dr. I. Arcavi, and Prof. Dan Maoz for their supports to keep this research going over the recent difficult situation around the globe.

MCL thanks Dr. P.-E. Tremblay and Dr. N. Gentile-Fusillo for cross-checking some data.

This research has made use of the Spanish Virtual Observatory (<http://svo.cab.inta-csic.es>) supported from the Spanish MICINN/FEDER through grant AyA2017-84089.

This work has made use of data from the European Space Agency (ESA) mission *Gaia* (<https://www.cosmos.esa.int/gaia>), processed by the *Gaia* Data Processing and Analysis Consortium (DPAC, <https://www.cosmos.esa.int/web/gaia/dpac/consortium>). Funding for the DPAC has been provided by national

institutions, in particular the institutions participating in the *Gaia* Multilateral Agreement.

## DATA AVAILABILITY

The source code underlying this article are available on Github and Zenodo, at <https://github.com/cylammarco/WDPHOTTools>, <https://doi.org/10.5281/zenodo.6570263>. The data and scripts for generating all the figures and analysis in this article, and the article itself, can be found at [https://github.com/cylammarco/WDPHOTTools\\_article](https://github.com/cylammarco/WDPHOTTools_article).

The comparison data from Gentile Fusillo et al. (2021) can be found in the public domain at <https://cdsarc.cds.unistra.fr/viz-bin/cat/J/MNRAS/508/3877>.

The filter profile used in this work can be found in the public domain at <http://svo2.cab.inta-csic.es/theory/fps3/>.

The white dwarf theoretical spectra can be found in the public domain at <http://svo2.cab.inta-csic.es/theory/newov2/index.php?models=koester2>.

The Montreal models used in this work can be found in the public domain at <https://www.astro.umontreal.ca/~bergeron/CoolingModels/>.

The BASTI models used in this work can be found in the public domain at <http://albione.oa-teramo.inaf.it/>.

The LPCODE models used in this work can be found in the public domain at <http://evolgroup.fcaglp.unlp.edu.ar/TRACKS/tracks.html>.

The GENEVA stellar evolution models used in this work can be found in the public domain at [https://obswww.unige.ch/Research/evol/tables\\_grids2011/](https://obswww.unige.ch/Research/evol/tables_grids2011/).

The PARSEC stellar evolution models used in this work can be found in the public domain at <http://dx.doi.org/10.5281/zenodo.61584>.

The MIST stellar evolution models used in this work can be found in the public domain at [http://waps.cfa.harvard.edu/MIST/model\\_grids.html](http://waps.cfa.harvard.edu/MIST/model_grids.html).

## REFERENCES

- Althaus L. G., García-Berro E., Isern J., Córscico A. H., Rohrmann R. D., 2007, *A&A*, **465**, 249
- Althaus L. G., Panei J. A., Miller Bertolami M. M., García-Berro E., Córscico A. H., Romero A. D., Kepler S. O., Rohrmann R. D., 2009, *ApJ*, **704**, 1605
- Althaus L. G., Córscico A. H., Isern J., García-Berro E., 2010a, *A&A Rev.*, **18**, 471
- Althaus L. G., García-Berro E., Renedo I., Isern J., Córscico A. H., Rohrmann R. D., 2010b, *ApJ*, **719**, 612
- Althaus L. G., Miller Bertolami M. M., Córscico A. H., 2013, *A&A*, **557**, A19
- Althaus L. G., Camisassa M. E., Miller Bertolami M. M., Córscico A. H., García-Berro E., 2015, *A&A*, **576**, A9
- Althaus L. G., De Gerónimo F., Córscico A., Torres S., García-Berro E., 2017, *A&A*, **597**, A67
- Andrews J. J., Agüeros M. A., Gianninas A., Kilic M., Dhital S., Anderson S. F., 2015, *ApJ*, **815**, 63
- Bailer-Jones C. A. L., Rybizki J., Fournesneau M., Demleitner M., Andrae R., 2021, *AJ*, **161**, 147
- Barbary K., 2016, Extinction V0.3.0, Zenodo, [doi:10.5281/zenodo.804967](https://doi.org/10.5281/zenodo.804967)
- Barrientos M., Chanamé J., 2021, *ApJ*, **923**, 181
- Bédard A., Bergeron P., Brassard P., Fontaine G., 2020, *ApJ*, **901**, 93
- Bedin L. R., King I. R., Anderson J., Piotto G., Salaris M., Cassisi S., Serenelli A., 2008, *ApJ*, **678**, 1279

<sup>17</sup> <https://warwick.ac.uk/fac/sci/physics/research/astro/people/tremblay/modelgrids>

- Bergeron P., Wesemael F., Beauchamp A., 1995, *PASP*, **107**, 1047
- Bergeron P., et al., 2011, *ApJ*, **737**, 28
- Bergeron P., Dufour P., Fontaine G., Coutu S., Blouin S., Genest-Beaulieu C., Bédard A., Rolland B., 2019, *ApJ*, **876**, 67
- Blouin S., Kowalski P. M., Dufour P., 2017, *ApJ*, **848**, 36
- Blouin S., Dufour P., Allard N. F., 2018, *ApJ*, **863**, 184
- Bressan A., Marigo P., Girardi L., Salasnich B., Dal Cero C., Rubele S., Nanni A., 2012, *MNRAS*, **427**, 127
- Bressan A., Marigo P., Girardi L., Nanni A., Rubele S., 2013, in European Physical Journal Web of Conferences. p. 03001 ([arXiv:1301.7687](#)), [doi:10.1051/epjconf/20134303001](#)
- Camisassa M. E., Althaus L. G., Córscico A. H., Vinyoles N., Serenelli A. M., Isern J., Miller Bertolami M. M., García-Berro E., 2016, *ApJ*, **823**, 158
- Camisassa M. E., Althaus L. G., Rohrmann R. D., García-Berro E., Torres S., Córscico A. H., Wachlin F. C., 2017, *ApJ*, **839**, 11
- Camisassa M. E., et al., 2019, *A&A*, **625**, A87
- Catalán S., 2015, in Dufour P., Bergeron P., Fontaine G., eds, Astronomical Society of the Pacific Conference Series Vol. 493, 19th European Workshop on White Dwarfs. p. 325
- Catalán S., Isern J., García-Berro E., Ribas I., 2008a, *MNRAS*, **387**, 1693
- Catalán S., Isern J., García-Berro E., Ribas I., Allende Prieto C., Bonanos A. Z., 2008b, *A&A*, **477**, 213
- Chabrier G., 2003, *PASP*, **115**, 763
- Chandra V., Hwang H.-C., Zakamska N. L., Budavári T., 2020, *MNRAS*, **497**, 2688
- Chen Y., Girardi L., Bressan A., Marigo P., Barbieri M., Kong X., 2014, *MNRAS*, **444**, 2525
- Choi J., Dotter A., Conroy C., Cantiello M., Paxton B., Johnson B. D., 2016, *ApJ*, **823**, 102
- Cummings J. D., Kalirai J. S., Tremblay P. E., Ramirez-Ruiz E., 2016, *ApJ*, **818**, 84
- Cummings J. D., Kalirai J. S., Tremblay P. E., Ramirez-Ruiz E., Choi J., 2018, *ApJ*, **866**, 21
- D'Antona F., Mazzitelli I., 1989, *ApJ*, **347**, 934
- Deloye C. J., Bildsten L., 2002, *ApJ*, **580**, 1077
- Dotter A., 2016, *ApJS*, **222**, 8
- Ekström S., et al., 2012, *A&A*, **537**, A146
- El-Badry K., Rix H.-W., Weisz D. R., 2018, *ApJ*, **860**, L17
- Fantini N. J., Côté P., McConachie A. W., 2020, *ApJ*, **900**, 139
- Fitzpatrick E. L., 1999, *PASP*, **111**, 63
- Fontaine G., Brassard P., Bergeron P., 2001, *PASP*, **113**, 409
- Foreman-Mackey D., Hogg D. W., Lang D., Goodman J., 2013, *PASP*, **125**, 306
- Gaia Collaboration et al., 2021a, *A&A*, **649**, A1
- Gaia Collaboration et al., 2021b, *A&A*, **649**, A6
- García-Berro E., Althaus L. G., Córscico A. H., Isern J., 2008, *ApJ*, **677**, 473
- García-Berro E., et al., 2010, *Nature*, **465**, 194
- Genest-Beaulieu C., Bergeron P., 2019a, *ApJ*, **871**, 169
- Genest-Beaulieu C., Bergeron P., 2019b, *ApJ*, **882**, 106
- Gentile Fusillo N. P., et al., 2021, *MNRAS*, **508**, 3877
- Georgy C., Ekström S., Granada A., Meynet G., Mowlavi N., Eggenberger P., Maeder A., 2013a, *A&A*, **553**, A24
- Georgy C., et al., 2013b, *A&A*, **558**, A103
- Giammichele N., Bergeron P., Dufour P., 2012, *ApJS*, **199**, 29
- Haft M., Raffelt G., Weiss A., 1994, *ApJ*, **425**, 222
- Harris H. C., et al., 2006, *AJ*, **131**, 571
- Harris C. R., et al., 2020, *Nature*, **585**, 357
- Heyl J., Caiazzo I., Richer H. B., 2022, *ApJ*, **926**, 132
- Holberg J. B., Bergeron P., 2006, *AJ*, **132**, 1221
- Iben I. J., Tutukov A. V., 1984, *ApJ*, **282**, 615
- Itoh N., Hayashi H., Nishikawa A., Kohyama Y., 1996, *ApJS*, **102**, 411
- Kalirai J. S., Saul Davis D., Richer H. B., Bergeron P., Catelan M., Hansen B. M. S., Rich R. M., 2009, *ApJ*, **705**, 408
- Kepler S. O., Koester D., Pelisoli I., Romero A. D., Ourique G., 2021, *MNRAS*, **507**, 4646
- Kilic M., Stanek K. Z., Pinsonneault M. H., 2007, *ApJ*, **671**, 761
- Kippenhahn R., Weigert A., Weiss A., 2013, *Stellar Structure and Evolution*, [doi:10.1007/978-3-642-30304-3](#).
- Knox R. A., Hawkins M. R. S., Hambly N. C., 1999, *MNRAS*, **306**, 736
- Koester D., 2010, *Mem. Soc. Astron. Italiana*, **81**, 921
- Kowalski P. M., Saumon D., 2006, *ApJ*, **651**, L137
- Kroupa P., 2001, *MNRAS*, **322**, 231
- Lam M. C., 2017, in Tremblay P. E., Gaensicke B., Marsh T., eds, Astronomical Society of the Pacific Conference Series Vol. 509, 20th European White Dwarf Workshop. p. 25 ([arXiv:1702.02187](#))
- Lam M. C., et al., 2019, *MNRAS*, **482**, 715
- Lam M. C., Hambly N. C., Lodieu N., Blouin S., Harvey E. J., Smith R. J., Gálvez-Ortiz M. C., Zhang Z. H., 2020, *MNRAS*, **493**, 6001
- Lauffer G. R., Romero A. D., Kepler S. O., 2018, *MNRAS*, **480**, 1547
- Leggett S. K., Ruiz M. T., Bergeron P., 1998, *ApJ*, **497**, 294
- Liebert J., Dahn C. C., Gresham M., Strittmatter P. A., 1979, *ApJ*, **233**, 226
- Liebert J., Dahn C. C., Monet D. G., 1988, *ApJ*, **332**, 891
- Liebert J., Dahn C. C., Monet D. G., 1989, *The Luminosity Function of White Dwarfs in the Local Disk and Halo*. p. 15, [doi:10.1007/3-540-51031-1\\_287](#)
- Miller D. R., Caiazzo I., Heyl J., Richer H. B., Tremblay P.-E., 2022, *ApJ*, **926**, L24
- Moehler S., Koester D., Zoccali M., Ferraro F. R., Heber U., Napiwotzki R., Renzini A., 2004, *A&A*, **420**, 515
- Mowlavi N., Eggenberger P., Meynet G., Ekström S., Georgy C., Maeder A., Charbonnel C., Eyer L., 2012, *A&A*, **541**, A41
- Munn J. A., et al., 2017, *AJ*, **153**, 10
- Noh H.-R., Scalo J., 1990, *ApJ*, **352**, 605
- Oswalt T. D., Smith J. A., 1995, *On the Luminosity Function of White Dwarfs in Wide Binaries*. p. 24, [doi:10.1007/3-540-59157-5\\_168](#)
- Panei J. A., Althaus L. G., Chen X., Han Z., 2007, *MNRAS*, **382**, 779
- Paxton B., Bildsten L., Dotter A., Herwig F., Lesaffre P., Timmes F., 2011, *ApJS*, **192**, 3
- Paxton B., et al., 2013, *ApJS*, **208**, 4
- Paxton B., et al., 2015, *ApJS*, **220**, 15
- Renedo I., Althaus L. G., Miller Bertolami M. M., Romero A. D., Córscico A. H., Rohrmann R. D., García-Berro E., 2010, *ApJ*, **717**, 183
- Rolland B., Bergeron P., Fontaine G., 2018, *ApJ*, **857**, 56
- Rowell N., 2013, *MNRAS*, **434**, 1549
- Rowell N., Hambly N. C., 2011, *MNRAS*, **417**, 93
- Salaris M., Domínguez I., García-Berro E., Hernanz M., Isern J., Mochkovitch R., 1997, *ApJ*, **486**, 413
- Salaris M., Serenelli A., Weiss A., Miller Bertolami M., 2009, *ApJ*, **692**, 1013
- Salaris M., Cassisi S., Pietrinferni A., Kowalski P. M., Isern J., 2010, *ApJ*, **716**, 1241
- Schlafly E. F., Finkbeiner D. P., 2011, *ApJ*, **737**, 103
- Schmidt M., 1959, *ApJ*, **129**, 243
- Shaviv G., Kovetz A., 1976, *A&A*, **51**, 383
- Temmink K. D., Toonen S., Zapartas E., Justham S., Gänsicke B. T., 2020, *A&A*, **636**, A31
- Tremblay P. E., Bergeron P., 2009, *ApJ*, **696**, 1755
- Tremblay P. E., Bergeron P., Gianninas A., 2011, *ApJ*, **730**, 128
- Virtanen P., et al., 2020, *Nature Methods*, **17**, 261
- Williams K. A., Bolte M., Koester D., 2009, *ApJ*, **693**, 355
- Winget D. E., Hansen C. J., Liebert J., van Horn H. M., Fontaine G., Nather R. E., Kepler S. O., Lamb D. Q., 1987, *ApJ*, **315**, L77
- Wood M. A., 1992, *ApJ*, **386**, 539
- Zhao J. K., Oswalt T. D., Willson L. A., Wang Q., Zhao G., 2012, *ApJ*, **746**, 144
- Zuckerman B., Xu S., Klein B., Jura M., 2013, *ApJ*, **770**, 140

This paper has been typeset from a  $\text{\LaTeX}$  file prepared by the author.